



Magnetic fidelity of lunar samples and implications for an ancient core dynamo

Sonia M. Tikoo*, Benjamin P. Weiss, Jennifer Buz, Eduardo A. Lima, Erin K. Shea, Gabriela Melo, Timothy L. Grove

Department of Earth, Atmospheric, and Planetary Sciences, Massachusetts Institute of Technology, Cambridge, MA, USA

ARTICLE INFO

Article history:

Received 25 November 2011

Received in revised form

4 May 2012

Accepted 20 May 2012

Keywords:

lunar paleomagnetism

AF demagnetization

paleointensity

lunar dynamo

anhysteretic remanence

magnetic anisotropy

ABSTRACT

Some lunar rocks have stable magnetizations that provide compelling evidence for an ancient lunar core dynamo. However, a longstanding problem has been interpreting the unstable alternating field (AF) demagnetization behavior observed in the remaining majority of the Apollo lunar sample suite. Similar unstable behavior has also been observed for many meteorites. It is unclear whether the behavior of these samples indicates that they formed in the absence of an ancient magnetizing field or whether they simply have poor magnetic recording properties. It is necessary to distinguish between these two possibilities in order to determine whether paleomagnetic fields were present on a sample's parent body. To address this issue, we analyzed five samples whose rock magnetic properties span the full suite of observed demagnetization behaviors: mare basalts 15556, 15016, 12017, 10020, and troctolite 76535. We demonstrate that the effects of spurious anhysteretic remanent magnetization (ARM) during AF demagnetization, in combination with multidomain magnetic carriers and magnetic remanence anisotropy, are likely responsible for the apparently poor magnetic behavior of many lunar samples. Therefore, the unstable AF demagnetization behavior observed for many lunar samples is not alone sufficient for ruling out the presence of an ancient lunar core dynamo. Nevertheless, spurious ARM may explain the observation of surprisingly high ($\geq 1 \mu\text{T}$) Apollo-era paleointensity measurements for samples thought to have formed after the cessation of a lunar core dynamo ($< 1.5 \text{ Ga}$).

© 2012 Elsevier B.V. All rights reserved.

1. Introduction

A central question in lunar science is whether the Moon fully differentiated and formed a liquid metallic core. Moment of inertia data (Konopliv et al., 1998) and the lunar induced magnetic dipole moment (Hood et al., 1999) support the existence of a 220–450 km radius iron core, while Apollo seismic data provide evidence for a 240 km radius solid inner core (Weber et al., 2011), surrounded by a 330–365 km radius liquid outer core (Garcia et al., 2010; Weber et al., 2011). Magnetic studies provide another means to test for a lunar core through the identification of a paleomagnetic field: the detection of remanent magnetization in the lunar crust (Dyal et al., 1970) and in returned Apollo samples (Fuller and Cisowski, 1987) indicate that the Moon may have once possessed a dynamo magnetic field and, by implication, a molten, advecting metallic core (Garrick-Bethell et al., 2009; Shea et al., 2012). The existence of an ancient lunar dynamo is broadly consistent with a high-temperature lunar origin

(Pritchard and Stevenson, 2000; Runcorn, 1996). It also would have implications for the physics of dynamo generation because a prolonged and strong lunar field may require nontraditional power sources (Dwyer et al., 2011; Le Bars et al., 2011; Wiczeorek et al., 2006; Wiczeorek et al., 2012).

Although it has been known for decades that lunar rocks are magnetized, only recent studies have clearly determined that the magnetizing fields resulted from a core dynamo rather than from other field-generating mechanisms. In particular, a key proposed alternative to the core dynamo hypothesis is that lunar paleo-fields were transiently produced or amplified by currents in meteoroid impact-generated plasmas (Hood and Artemieva, 2008; Srnka, 1977). To address this ambiguity, Garrick-Bethell et al. (2009) and Shea et al. (2012) analyzed the paleomagnetism of samples unlikely to have recorded any impact-generated fields, the 4.2 billion year old (Ga) lunar troctolite 76535 and the 3.7 Ga mare basalt 10020. These rocks cooled from their Curie points to ambient temperatures over timescales greatly exceeding the expected duration of even the longest lived impact-generated magnetic fields (lasting $\sim 1 \text{ day}$) (Garrick-Bethell et al., 2009). These samples exhibit no petrographic evidence for shock effects (peak pressures $< 5 \text{ GPa}$), demonstrating that they are unlikely to have recorded transient magnetic fields via the shock remanent

* Correspondence to: 77 Massachusetts Avenue 54–825, Cambridge, MA 02139, USA. Tel.: +1 617 324 3935; fax: +1 617 258 7401.

E-mail address: smtikoo@mit.edu (S.M. Tikoo).

magnetization (SRM) process. Both samples contain a natural remanent magnetization (NRM) with a high coercivity component that is unidirectional across mutually oriented subsamples and which monotonically decays to the origin during demagnetization experiments (Garrick-Bethell et al., 2010; Shea et al., 2012). The stable magnetization components of 76535 and 10020 were acquired in fields of at least $1\ \mu\text{T}$ and probably several tens of μT (Garrick-Bethell et al., 2010; Shea et al., 2012). The lower end of this range is consistent with the expected $\sim 15\text{--}20\ \mu\text{T}$ upper limit for surface fields from an ancient lunar dynamo operating in a small ($\sim 300\text{--}400\ \text{km}$ radius) (Wieczorek et al., 2006; Dwyer et al., 2011; Le Bars et al., 2011). These data collectively suggest that the characteristic magnetization components in these samples are thermoremanent magnetization (TRM) obtained by cooling from the Curie point in the presence of a stable long-lived paleofield like that from a core dynamo.

The problem addressed in the present study is that the stable NRMs of 76535 and 10020 are exceptional when compared to other lunar samples. Most lunar rocks subjected to paleomagnetic studies display low fidelity NRM behavior during alternating field (AF) demagnetization experiments, characterized by non-monotonic decline of magnetization intensity and rapidly varying magnetization directions (Brecher, 1976; Hoffman and Banerjee, 1975). Such behavior makes it difficult to determine whether the observed magnetization was acquired in the presence or absence of a core dynamo field. The AF demagnetization procedure itself has been proposed to be responsible for much of this behavior. A frequent problem is that samples acquire spurious (i.e., unintended) anhysteretic remanent magnetization (ARM), which manifests as unstable moment directions and non-monotonic changes in NRM intensity during a series of AF steps [see Fig. 1 of Weiss et al. (2010)]. Another less common problem which may result in poor AF demagnetization behavior is the acquisition of gyroremanent magnetization (GRM) (Hu et al., 1998; Stephenson, 1980, 1993). GRM is a laboratory-produced component specific to single-domain-like particles that is acquired perpendicularly to the preferred easy axis orientation as well as to the axis of the last AF application (Dunlop and Ozdemir, 1997) and grows monotonically with peak AC field during AF demagnetization [see Fig. S5 of Garrick-Bethell et al. (2009)].

ARM noise is generated by the presence of even harmonics in the AF waveform during demagnetization (Collinson, 1983) due to harmonic distortion in oscillator and amplifier stages or spurious waveforms appearing at non-harmonic frequencies caused by interference (Figs. 1a, S1, and S2). The sum of the fundamental wave and the second harmonic or another contaminating frequency often creates asymmetry of the positive and negative peak values of the waveform, leading to the acquisition of ARM (see Supplementary material). This unintended ARM can be acquired along all three orthogonal axes by grains with coercivities up to that of the peak AC field of the AF step. Depending on the stability of the AF waveform spectrum, repeat AF applications at the same peak AC field may produce scatter in the NRM direction, suggesting that spurious ARM results from noise in the AF waveform and is not readily predictable. The magnitude of spurious ARM typically increases with AF amplitude because the magnitude of the second harmonic itself increases with AF amplitude.

Kamacite- and taenite-bearing materials like lunar rocks and many meteorites are primarily multidomain due to the small single domain stability range of these minerals. Spurious ARM is especially problematic for multidomain samples because they are dominated by low coercivity grains (e.g. Nagata et al., 1973; Weiss et al., 2010): as demagnetization proceeds to higher AF amplitudes, the magnitude of the primary magnetization in the sample decreases while the net moment becomes increasingly

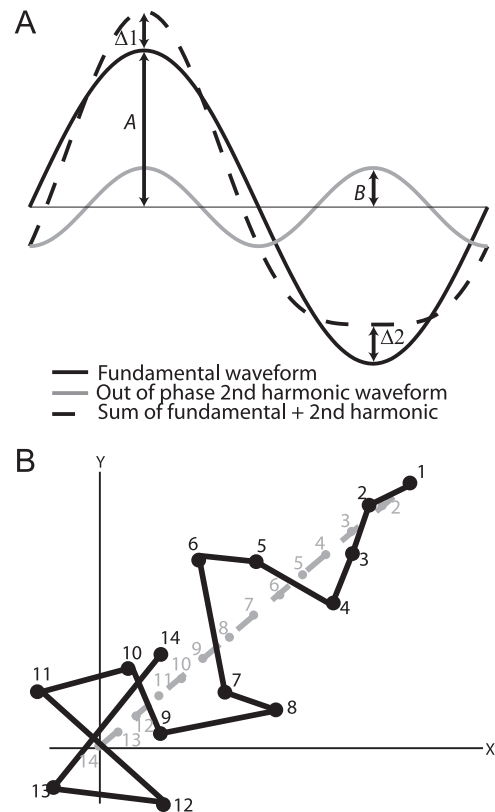


Fig. 1. Cause and effects of spurious ARM. (A) Generation of spurious ARM as a result of the summation of the fundamental AF waveform component of amplitude A with its second harmonic of amplitude B . Modified from Collinson (1983). $\Delta 1$ represents the increase in amplitude of the positive peak whereas $\Delta 2$ represents the increase in amplitude of the negative peak. Note that for a fixed amplitude ratio A/B between the harmonics, $\Delta 1$ and $\Delta 2$ are proportional to A (for the relative phases depicted here, $\Delta 1$ and $\Delta 2$ are in fact equal to the amplitude of the second harmonic; for other cases see Fig. S1). Therefore, the effective bias field changes for each period during the ramp-down of an AF application. (B) Schematic effects of spurious ARM on a theoretical AF demagnetization. The light gray line and points show an ideal scenario of NRM being stepwise demagnetized with NRM trending toward the origin. The black line and points show AF demagnetization affected by spurious ARM acquired during demagnetization. Numbers next to data points correspond to AF steps during the demagnetization experiment.

overpowered by spurious ARM acquired by low-coercivity grains (Fig. 1b). On the other hand, spurious ARM is much less of a problem in terrestrial paleomagnetic studies because iron oxides like magnetite and hematite much more commonly form pseudo single domain and smaller grains. The lack of noticeable adverse effects caused by nonideal AF demagnetization in terrestrial samples likely accounts for why the full implications of spurious ARM for paleomagnetic studies have not been previously appreciated.

Another related source of unstable AF demagnetization has been ascribed to “textural remanence” in which the NRM is controlled by magnetic anisotropy resulting from foliated or lineated magnetic fabrics in samples. Such fabrics may originate from shock or primary igneous processes. These effects can be dramatically expressed as pinning of the NRM vector during demagnetization (zig-zag demagnetization) along an axial direction or within a plane (Brecher, 1976, 1977; Hoffman and Banerjee, 1975).

Unstable demagnetization behavior, observed in many lunar samples as well as iron-bearing meteorites (Table S1), makes it difficult to pinpoint the origin of magnetization in these samples. Therefore, it is important to assess the magnetic recording fidelity of such samples before attempting to ascertain whether they

were formed in the presence or absence of a dynamo field. With this goal, we studied the AF demagnetization behavior and magnetic recording capacities of low fidelity mare basalts 15556, 15016, and 12017 which were previously observed to exhibit spurious AF demagnetization behavior, as well as high fidelity samples 76535 (Garrick-Bethell et al., 2009) and 10020 (Shea et al., 2012). We show that the unstable demagnetization behaviors observed for 15556, 15016, and 12017 likely result from the combined effects of multidomain magnetic carriers, magnetic anisotropy, and spurious ARM. We conclude that while the unstable demagnetization data for 15556, 15016, and 12017 clearly do not provide evidence for the presence of a lunar dynamo at 3.2–3.4 Ga, they also do not require the absence of a dynamo-generated magnetic field on the Moon at this time.

2. Description of analyzed lunar samples

2.1. Petrologic descriptions

15556 is a fine-grained, highly vesicular, olivine-normative basalt (Meyer, 2008) with an $^{40}\text{Ar}/^{39}\text{Ar}$ age of ~ 3.4 Ga (Kirsten et al., 1972). Our petrographic analyses (see Supplementary material) found no evidence of shock, implying peak shock pressures < 5 GPa: plagioclase crystals do not show any mechanical twinning, fracturing, or alteration to maskelynite, and there is no undulatory extinction in olivine (Fig. S3a). Thermomagnetic curves identified kamacite ($\text{Fe}_{0.94-0.96}\text{Ni}_{0.04-0.06}$) as the main ferromagnetic constituent in 15556 (Nagata et al., 1972, 1973). Our elemental abundance analyses of metal grains using a JEOL-JXA-8200 electron microprobe at the Massachusetts Institute of Technology found that kamacite occurs as isolated 2–30 μm diameter blebs ($\text{Fe}_{0.94}\text{Ni}_{0.06}$) as well as ~ 5 μm diameter grains of nearly pure iron intergrown with troilite (Table S2).

15016 is a medium-grained, highly vesicular, olivine-normative basalt (Meyer, 2008) with Rb/Sr and $^{40}\text{Ar}/^{39}\text{Ar}$ ages of 3.3–3.4 Ga (Evensen et al., 1973; Kirsten et al., 1972). 15016 does not show any petrographic evidence of shock (peak shock pressure < 5 GPa) (Fig. S3b). Our microprobe analyses identified 2–3 μm diameter metallic iron associated with troilite as well as 10 μm diameter free kamacite ($\text{Fe}_{0.87-0.93}\text{Ni}_{0.07-0.13}$) (Table S2).

12017 is a medium-grained pigeonite basalt (Meyer, 2008; Warner, 1970) lacking shock features (Fig. S3c) with an $^{40}\text{Ar}/^{39}\text{Ar}$ age of 3.2 Ga (Horn et al., 1975). The basalt is coated on one side with an impact glass estimated to be ~ 4 –20 thousand years (ky) old (Fleischer et al., 1971; Morrison et al., 1973) (Table S2). The subsamples used in our paleomagnetic experiments were taken from both basaltic (12a2, 12a1c, and 13b1) and glass (12b, 13a2, and 59) lithologies. In the basalt portion, our microprobe analysis identified 3–5 μm metallic iron blebs in troilite as well as 50 μm free metal grains with composition $\text{Fe}_{0.99}\text{Ni}_{0.01}$. The glass portion contained 20 μm blebs of iron phosphide with ≤ 1 μm iron sulfide inclusions. Furthermore, ≤ 1 μm blebs of kamacite were distributed throughout the glass (Table S2). The latter grains were too small for accurate quantitative elemental analyses.

10020 is an apparently unshocked (peak shock pressure < 5 GPa) (Fig. S1d), fine-grained low-K ilmenite basalt (Kramer et al., 1977; Meyer, 2008) with an $^{40}\text{Ar}/^{39}\text{Ar}$ age of 3.72 Ga (Geiss et al., 1977; Guggisberg et al., 1979; Shea et al., 2012). Our microprobe analysis identified 0.1–5 μm metallic iron (negligible Ni content) blebs in troilite (Table S2).

76535 is an apparently unshocked (peak shock pressure < 5 GPa), coarse-grained troctolite (Meyer, 2008) dated to 4.2 Ga using a variety of chronometers [see Garrick-Bethell et al. (2009)]. The sample contains kamacite and taenite as free blebs and as inclusions in plagioclase [see Garrick-Bethell et al. (2009)].

2.2. Domain state

We assessed the domain state of samples 15556, 15016, 12017, and 10020 by measuring hysteresis loops and first order reversal curves [FORCs; see Pike et al. (1999)] (see Supplementary material). Ratios of saturation remanent magnetization (M_{rs}) to saturation magnetization (M_s) and remanent coercivity (H_{cr}) to coercivity (H_c) (Dunlop, 2002a, b) and FORC distributions indicate that all four samples are predominantly multidomain (Figs. S4 and S5 and Table S3), consistent with previous studies (Cournede et al., 2012; Gattacceca et al., 2010; Nagata et al., 1972, 1973; Pearce et al., 1973; Shea et al., 2012). Previous hysteresis studies also indicated a dominantly multidomain grain size for 76535 (Garrick-Bethell et al., 2009) (Table S3). While 10020 and 76535 have an average grain size in the multidomain range, their hysteresis parameters (higher M_{rs}/M_s , lower H_{cr}/H_c) suggest that they are less coarse-grained than samples with poor NRM demagnetization behavior (15556, 15016, and the 12017 basalt; see Sections 3.2–3.4) (Fig. 2). This relationship is confirmed by our FORC analyses, which indicate that 10020 has an additional population of higher coercivity grains relative to 15556, 15016, and the 12017 basalt (Fig. S5) as well as our coercivity spectra (see below).

2.3. Rock magnetic studies

We conducted a variety of rock magnetic experiments on 15556, 15016, 12017, and 10020 to characterize magnetostatic interactions, their coercivity spectra, and their median destructive fields (MDFs) (see Supplementary material). Paleomagnetic and rock magnetic remanence experiments were conducted using a 2G Enterprises Superconducting Rock Magnetometer 755 equipped with automated sample handling and demagnetization equipment (Kirschvink et al., 2008) in a magnetically shielded room (field < 200 nT) housed in the MIT Paleomagnetism Laboratory (<http://web.mit.edu/paleomag>). The magnetometer has a sensitivity of to $\sim 1 \times 10^{-12}$ Am^2 , at least 2 orders of magnitude lower than nearly all magnetic moments measured here. Four

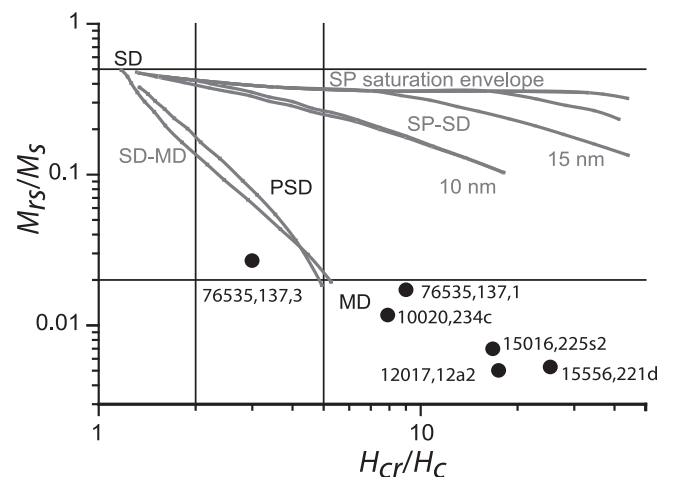


Fig. 2. Dunlop–Day plot of hysteresis parameters. The ordinate gives the magnitude of the saturation remanent magnetization (M_{rs}) divided by the magnitude of the saturation magnetization (M_s). The abscissa gives the remanent coercivity (H_{cr}) divided by the coercive force (H_c). Black circles designate sample positions. Straight black vertical and horizontal lines divide the plot into rectangular regions representing single domain (SD), pseudo-single domain (PSD), and multidomain (MD) regimes. Note that this plot was developed for magnetite-bearing samples and should only be used for a qualitative understanding of grain size trends for the kamacite-bearing samples shown here.

readings of magnetic moment were made and averaged for each measurement, and circular standard deviations were typically $< 2^\circ$. Samples which exhibit spurious AF demagnetization (15556, 15016, and basalt 12017; see [Supplementary material](#)) display lower remanent coercivities and median destructive fields for ARM and isothermal remanent magnetization (IRM) than 10020 and the 12017 glass, which have stable demagnetization patterns ([Supplementary material, Table S4 and Fig. S6](#)). These results are consistent with the hysteresis properties ([Section 2.2](#)), which suggest that low magnetic fidelity samples (i.e. 15556, 15016, and the 12017 basalt) contain a larger fraction of multidomain magnetic carriers than high fidelity samples 10020 and the 12017 glass (see [Section 4.3](#)).

The low remanent coercivities and MDFs of samples 15016 and the 12017 basalt mean that their putative primary TRM (if present) may have been partly demagnetized by shock during impact excavation, because shock pressures of just 2 GPa can demagnetize grains with coercivities up to ~ 30 mT ([Gattacceca et al., 2008](#)). On the other hand, higher coercivity samples like 10020 and the 12017 glass should still be able to retain some primary TRM (if present), even if they have experienced some shock effects.

3. Natural remanent magnetization

3.1. Methodology

We studied the NRM behavior of mutually oriented subsamples of 15556, 15016, 12017 (basalt and glass portions), and 10020. We used AF rather than thermal demagnetization because the former should more efficiently remove secondary IRM and SRM overprints which are blocked by coercivity rather than blocking temperature. Such overprints have been ubiquitously observed in lunar samples. Thermal demagnetization associated with the Thellier–Thellier paleointensity method is also disadvantageous because it typically causes alteration of the metallic magnetization carriers in lunar rocks.

All subsamples except those from 12017 were taken from the non-space-weathered interiors of their parent rocks. The samples were subjected to identical progressive three axis AF demagnetization sequences up to 85 mT, with some subsamples further demagnetized up to 290 mT. Antiparallel treatment orientations were not used due to sample mounting restrictions. We measured the magnetic moment after AF application in each of the three orthogonal (N, E, Z coordinate) directions and computed the final moments as the average of all measurements for each AF level [after [Garrick-Bethell et al. \(2009\)](#)] in order to reduce spurious ARM and GRM (see [Section 1](#)).

We used principal component analysis (PCA) ([Kirschvink, 1980](#)) to determine the best-fit directions for the magnetization components in each sample and the dANG/MAD test to qualitatively assess whether a magnetization component trends toward the origin [see [Lawrence et al. \(2008\)](#)]. This method compares the angular difference between a non-origin-constrained least squares fit of the NRM component and the centroid of the least squares fit (dANG) to the maximum angle of deviation (MAD) of the fit. Although this test is somewhat arbitrary because it does not assign a confidence interval to the hypothesis that the NRM component is origin-trending, we adopt it here in the absence of more robust statistical tests (see [Supplementary material](#)).

We tested for GRM acquisition in our samples following [Garrick-Bethell et al. \(2009\)](#) (see [Section 3.2](#) of their [Supplementary Online Material](#)). We found that GRM does not significantly contribute to the demagnetization behavior of our mare basalts (see [Supplementary material and Fig. S7](#)).

3.2. Summary of demagnetization results

All subsamples from 15556, 15016, and 12017 analyzed in this study exhibited unstable behavior during demagnetization of NRM ([Fig. 3](#)). Repeated AF steps at a single field level led to large changes in moment. This variability is certainly unrelated to the moment sensitivity of our magnetometer because repeat measurements (without intervening demagnetization) were essentially identical and the measured moments were at least two orders of magnitude above our instrument's detection limit. Furthermore, the magnetic fields inside our shielded room and AF coils are < 200 nT so the cause of unstable demagnetization cannot be induced moments or ARM acquired in a time-varying background field. Rather, as described below, the unstable AF behavior observed in our samples appears to be the product of spurious ARM and remanence anisotropy.

Low coercivity (LC) magnetization components blocked from to ~ 10 mT could be identified in 15 out of 17 subsamples. Only 4 out of 17 subsamples clearly had additional higher coercivity (HC) components, and even these were only blocked to low coercivities (< 25 mT) (see [Supplementary material, Table S5](#)). For sample 15556, which had three subsamples with clear HC components, both the LC and HC components of these subsamples were generally non-unidirectional with respect to each other ([Fig. S8](#)). One subsample, 15556,221c displayed a spectacular case of magnetic pinning where the moment flipped repeatedly between two antipodal directions during AF application up to 290 mT (see [Fig. 3b and S9](#)). For subsamples lacking easily identifiable HC components (the vast majority of subsamples), we fit nominal HC components in order to later demonstrate that this AF range yields paleointensity ranges with high uncertainties that make them indistinguishable from zero (null field) (see [Section 4.2](#)). Given this behavior, our NRM data for 15556, 15016, and 12017 clearly do not provide any evidence for the existence of an ancient lunar dynamo when these samples formed between 3.2 and 3.4 Ga.

4. Paleointensity studies

4.1. Introduction

A major goal of lunar paleomagnetism studies is to determine the paleointensity of the ancient magnetizing field. For the reasons described in [Section 3.1](#), we chose to use the nondestructive, AF-based ARM and IRM methods to estimate absolute paleointensities for the HC components of our samples (see [Supplementary material](#)). These methods are similar to those used for paleointensity studies during the Apollo era, allowing us to assess the meaning of these previous results in the context of the magnetic recording fidelity of the rocks.

4.2. NRM paleointensity results

Paleointensity results for sample 10020 provide robust evidence for Earth-strength fields on the Moon ([Shea et al., 2012](#)). However, most paleointensity experiments on 15556, 15016, and 12017 were inconclusive (see [Supplementary material](#)). Most subsamples either yielded formally negative (i.e., meaningless) paleointensities or had formal uncertainties exceeding their corresponding paleointensity values ([Table S7](#)) indicating that they are consistent with zero magnetizing field. These results, coupled with the noisy NRM demagnetization behavior observed for these samples, led us to examine their magnetic recording fidelity. Our goal was to determine whether certain samples are intrinsically incapable of stable AF demagnetization behaviors.

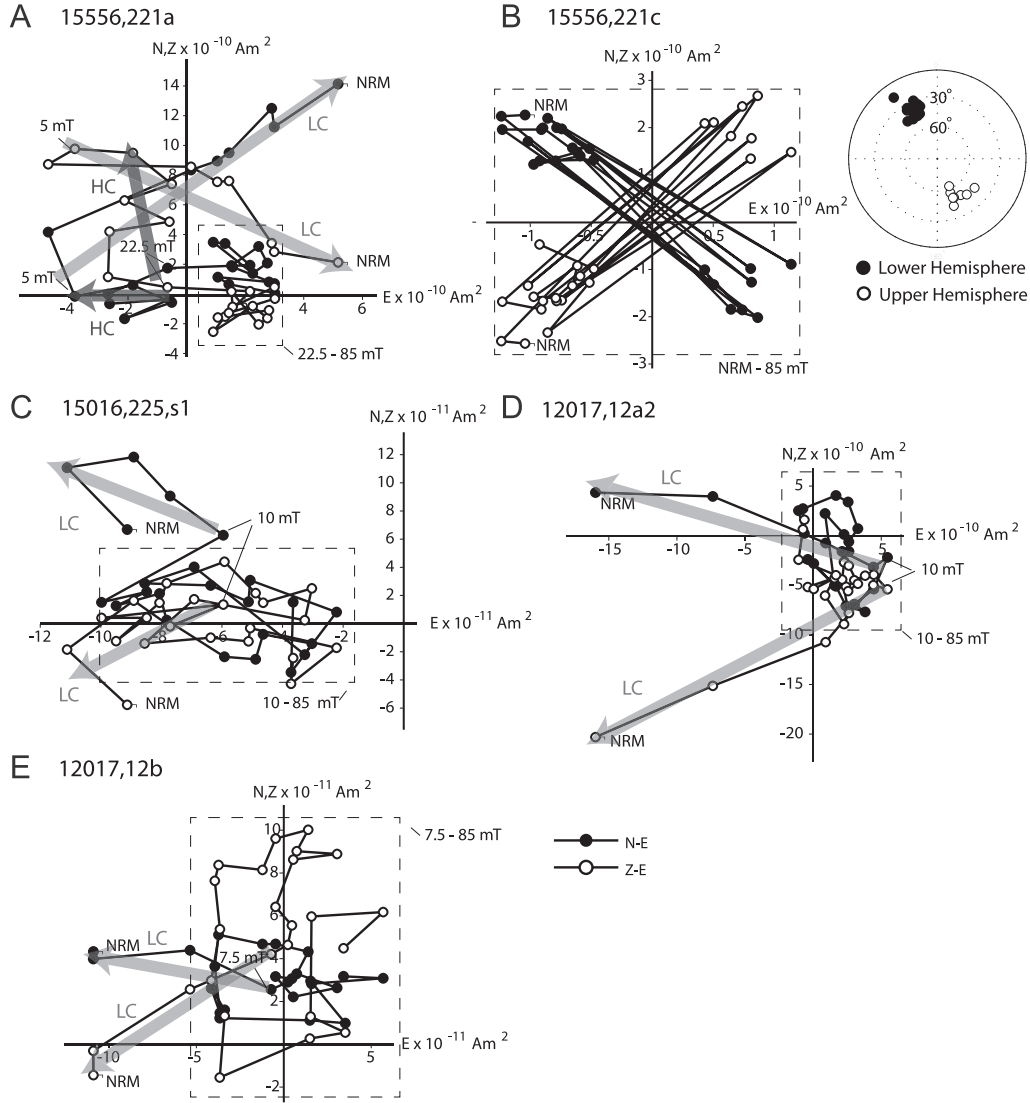


Fig. 3. NRM demagnetization data for lunar samples. Shown for each sample are two-dimensional projections of the NRM vector during AF demagnetization. Closed symbols represent end points of magnetization projected onto the horizontal (N and E) plane. Open symbols represent end points of magnetization projected onto the vertical (Z and E) plane. Peak fields for selected AF steps are labeled in mT. Low coercivity (LC) and high coercivity (HC) magnetization components are labeled and represented with light gray and dark gray arrows, respectively. (A) 15556,221a. (B) 15556,221c. Inset shows equal-area stereographic presentation of data. Data shown for this subsample have been downsampled to every fifth AF step and were not averaged using the Zijderveld–Dunlop method. For full demagnetization data see Fig. S7. (C) 15016,225s1. (D) basalt 12017,12a2. (E) glass sample 12017,12b.

If a sample has low magnetic recording fidelity, it cannot be used to determine whether a paleomagnetic field was present on its parent body.

4.3. Paleointensity limit tests

We conducted the following experiment to assess the magnetic recording fidelity of our samples. At least one subsample from each parent rock was imparted with a laboratory ARM using DC bias fields ranging from 3 μ T to 200 μ T and an AC field of 85 mT to simulate TRM acquisition at paleofields ranging from 2–150 μ T [using an TRM/ARM ratio of 1.34 measured for some lunar rocks; see Stephenson and Collinson (1974)]. We then used the ARM method to retrieve paleointensities for each applied lab field. A comparison of retrieved paleointensities against the applied (known) intensity that produced the laboratory remanence indicates the magnetic recording fidelity of a sample. This approach is analogous to a TRM experiment previously used for ordinary chondrites (Brecher and Leung, 1979). The closer a

retrieved paleointensity value is to the applied lab field intensity and its estimated uncertainty due to unstable AF behavior, the more likely a magnetization can be successfully retrieved using AF methods. We quantified this agreement as a function of applied field strength using two metrics that we call difference (D) and error (E):

$$D \equiv |L - I| / L \cdot 100\% \quad (1)$$

$$E \equiv W / L \cdot 100\% \quad (2)$$

The first metric quantifies the difference between the TRM-equivalent value of the applied laboratory field (L) and the retrieved paleointensity (I) (Fig. 4a). The second metric quantifies the error associated with the paleointensity measurement by comparing the width of the Student's t -test-derived 95% confidence interval (W) for the retrieved paleointensity to the magnitude of the applied laboratory field (see Supplementary material) (Fig. 4b). We used two metrics because it is possible for a retrieved paleointensity to be close in value to the applied

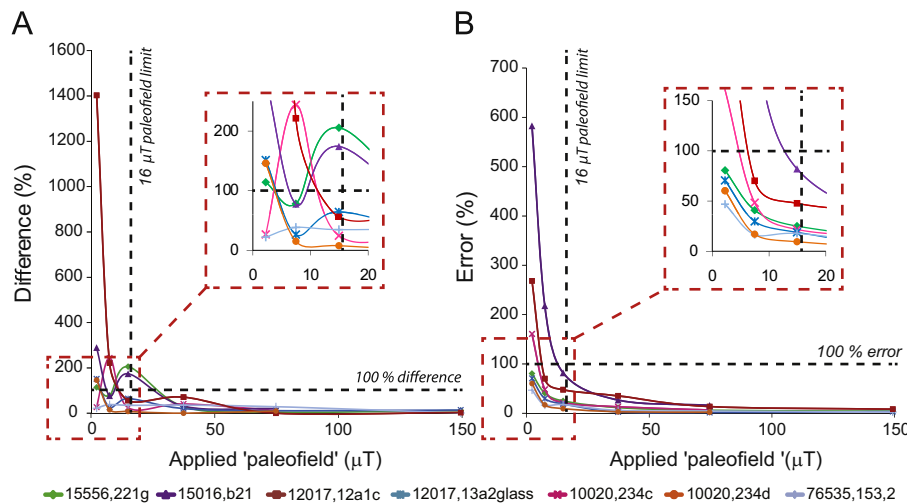


Fig. 4. Artificial paleointensity tests on lunar samples. (A) Difference and (B) error for retrieved paleointensities versus magnitude of applied laboratory field for samples 15556,221g (green diamonds), 15016,b21 (violet triangles), 12017,12a1c (maroon squares), 12017,13a2 (teal stars), 10020,234c (pink crosses), 10020,234d (orange circles), and 76535,153,2 (light blue pluses). See Section 4.3 for definitions. In (A), the dashed horizontal line denotes the threshold of 100% difference between the applied field and the retrieved paleointensity. In (B), the dashed horizontal marks the threshold where the width of the 95% confidence interval of the retrieved paleointensity is equal in magnitude to the applied laboratory field. Shown in both parts (A) and (B) is the 16 μT estimated maximum surface paleointensity limit for a dynamo generated by a 375 km radius lunar core in magnetostrophic balance (Wieczorek et al., 2006).

laboratory field (i.e., have a low value for D), but for the formal error associated with the experiment due to nonideal demagnetization behavior to be larger than the magnitude of the paleointensity (i.e., have a large value for E). Both metrics should have low values for a paleointensity to be considered high quality. Here we define a sample to be a good magnetic recorder at those field strengths for which the following conditions are satisfied: (a) there is less than 100% difference between the applied field and retrieved paleointensity and (b) there is less than 100% error associated with the measurement. These thresholds are somewhat arbitrary but are certainly generous towards poor recorders: it is virtually certain that samples that do not meet these thresholds are nonideal for paleointensity studies.

We found that AF demagnetization of magnetization produced in higher applied lab fields exhibited more ideal behavior than magnetization produced with weak fields (Fig. S10). Weak-field magnetizations were prone to spurious demagnetization, which in turn resulted in less accurate retrieved paleointensities during the experiment described in the preceding paragraph. We found that AF methods can retrieve TRM-equivalent fields down to 7 μT for 10020,234d and glass 12017,13a2, and as weak as 2 μT for 76535,153. By comparison, we could only retrieve TRM-equivalent fields down to 37 μT for basalts 15016,b21 and 15556,221g. Furthermore, heterogeneities in magnetic recording fidelity may exist within a single sample. For example, we found that we could retrieve TRM-equivalent paleointensities as weak as 7 μT from 10020,234d but only down to 15 μT for 10020,234c. This difference in recording fidelity is mirrored by observed differences in NRM demagnetization behavior between these two subsamples [compare Shea et al. (2012)'s Fig. S3A,C with their Fig. S3B]. Therefore, a computed paleointensity from a subsample should ideally only be compared with the field recording limit determined for the same subsample when assessing the reliability of paleointensity estimates. In summary, only high-fidelity samples such as 10020, 76535, or the 12017 glass are capable of stable AF demagnetization and providing reliable AF-based paleointensity values from the predicted weak fields ($< 16 \mu\text{T}$) from a lunar dynamo. Paleointensities from intermediate fidelity samples should be scrutinized subsample-by-subsample. AF-based paleointensity results from poor magnetic recorders

(e.g., 15016, 12017 basalt, and 15556) should be regarded with caution.

4.4. Implications for Apollo-era paleointensity methods

We have shown that nonideal AF demagnetization and inaccurate paleointensity determinations may be caused by spurious ARM. This conclusion led us to re-assess previous lunar paleointensity analyses conducted using AF-based techniques. The majority of IRM paleointensities acquired during the Apollo era used the NRM₂₀/sIRM₂₀ normalization method [termed the "REMc" method by Acton et al. (2007)] in which NRM AF demagnetized to 20 mT (TRM₂₀) was compared to sIRM AF demagnetized to 20 mT (sIRM₂₀) (Cisowski et al., 1983; Fuller and Cisowski, 1987). This method was used because many samples exhibited low-field ($< 10 \text{ mT}$) IRM overprints that would otherwise contaminate paleointensities derived from ratios of undemagnetized NRM and IRM. A major problem with this method is that highly multidomain lunar samples and synthetic samples displayed a non-linear relationship between laboratory TRM₂₀ to sIRM₂₀ when the TRM was applied in weak fields ($< 10 \mu\text{T}$) (Cisowski et al., 1983; Fuller and Cisowski, 1987). The reason for this behavior was left unexplained and led the authors to question the fidelity of the majority of Apollo-era paleointensity values.

Our results described above suggest this nonlinear behavior may be a manifestation of ARM noise. To test this hypothesis, we studied the relationship between laboratory ARM which was AF demagnetized to 20 mT (ARM₂₀) and sIRM₂₀ on the same subsamples used in the preceding section (see Supplementary material for further discussion of our methodology and results). We observed a nonlinear relationship between ARM₂₀ and sIRM₂₀ at ARM DC fields ranging from 3–200 μT (equivalent to TRM acquired at 2–150 μT) (Fig. 5a). For comparison, we examined the relationship between total ARM and total sIRM (i.e., that were not subsequently demagnetized) (ARM₀ and sIRM₀). In this case, we observed a linear relationship between ARM₀ and sIRM₀ (analogous to non-demagnetized TRM and sIRM) for almost all samples down to their recording limits (Fig. 5b). Given that we have shown that highly multidomain samples are extremely

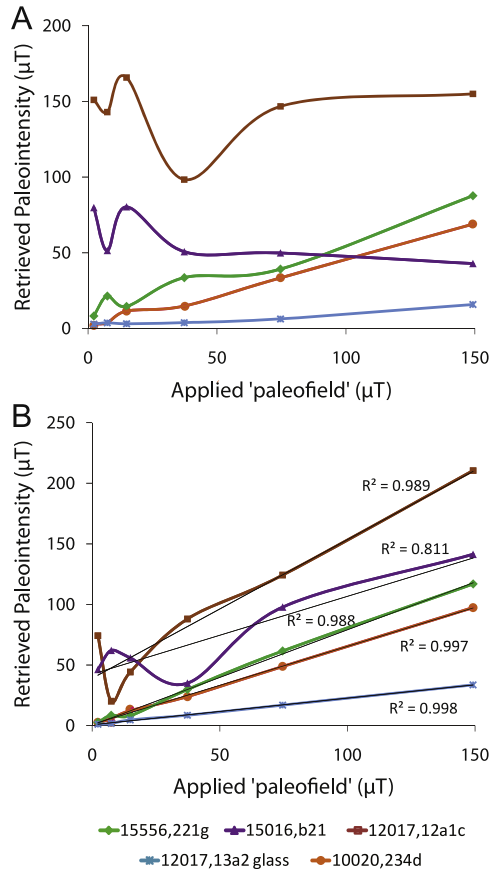


Fig. 5. Simulated paleointensity tests using the (A) $ARM_{20}/sIRM_{20}$ normalization method, (B) total $ARM/sIRM$ (i.e., without AF demagnetization). Plots show retrieved paleointensities versus applied laboratory fields. Featured samples are: 15556,221g (green diamonds), 15016,b21 (violet triangles), 12017,12a1c (maroon squares), 12017,13a2 (teal stars), and 10020,234d (orange circles).

susceptible to spurious ARM, we propose that the nonlinear relationship between ARM_{20} and IRM_{20} and between TRM_{20} and $sIRM_{20}$ observed by [Cisowski et al., 1983](#), [Fuller and Cisowski \(1987\)](#) and in our [Fig. 5a](#) is a manifestation of ARM noise introduced by the AF application used in these experiments. Unfortunately, this problem cannot be reconciled by simply computing ratios of undemagnetized NRM and $sIRM$ due to the ubiquitous presence of low coercivity overprints (typically secondary IRM) in lunar samples.

A related longstanding unsolved issue in lunar paleointensity studies observed specifically when using the REMc paleointensity method is that there appears to be a minimum paleofield ($NRM_{20}/sIRM_{20} \geq 3.6 \times 10^{-4}$, implying paleointensities $\geq 1 \mu T$) that has been retrieved, regardless of sample age ([Cisowski et al., 1983](#)). This minimum field, which is far stronger than nearly all putative field sources other than a core dynamo, is even observed in samples < 1.5 Ga in age when a dynamo is highly unlikely due to a lack of power sources [see [Dwyer et al., 2011](#); [Le Bars et al., 2011](#); [Stegman et al., 2003](#)]. Our results indicate that all AF-based paleointensity experiments will give highly inaccurate values if the field that magnetized the samples has a lower intensity than the minimum limit that can be retrieved due to ARM noise ([Fig. 6](#)). Specifically, when using the REMc normalization method, spurious ARM may inflate values for ARM_{20} , yielding high ($\geq 1 \mu T$) paleointensities for samples which may have nevertheless formed in a zero-field environment after the end of a lunar dynamo. This suggests that REMc paleointensity values measured for young samples with ages of several hundred Ma

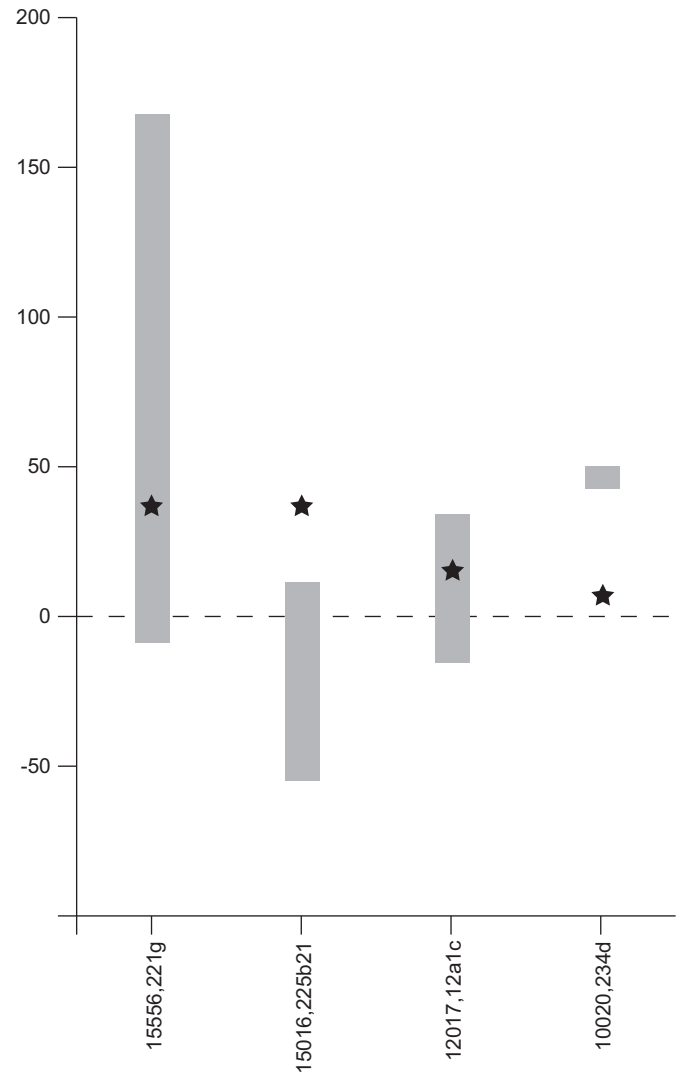


Fig. 6. Calculated paleointensities and paleofield recording limits measured for various lunar samples. Gray rectangles show the paleointensities (including formal uncertainties) computed for AF ranges of 23–85 mT for each sample (name listed along bottom axis) using the ARM and IRM methods. This range of AF fields was used to calculate paleointensities for this plot in order to avoid inclusion of possible low-coercivity overprints on samples. Paleointensity values reported for 10020 are from [Shea et al. \(2012\)](#). Black stars show the minimum paleofield required to retrieve accurate paleointensities using the ARM method.

may only be upper limits and should be reevaluated using more robust paleointensity techniques.

5. Zig-zag behavior

We have discussed the observation of unstable AF demagnetization behavior present during demagnetization of both NRM and induced ARM (as a proxy for TRM) in some lunar samples. Magnetic anisotropy studies on these samples may shed light on sources of the more ordered spurious behaviors that have been observed, like zig-zag demagnetization and pinning of magnetization directions. We next discuss how magnetic anisotropy in combination with spurious ARM may be responsible for these behaviors.

The flipping of the magnetic moment of sample 15556,221c between two nearly antipodal directions suggests that magnetic anisotropy is the source for zig-zag demagnetization. This is

because anisotropy preferentially constrains magnetization to easy axes and planes. We conducted ARM and IRM anisotropy of remanence experiments on various subsamples of basalts 15556, 15016, 12017, and 10020 (Tables S8 and S9). We applied ARM (DC field of 2 mT and AC field of 800 or 850 mT) and IRM (20 mT field) along all three orthogonal axes and solved for the principal axes of the anisotropy ellipsoids [following Stephenson et al. (1986)]. We averaged the results of each experiment (two ARM and two IRM experiments) for all samples except the 12017 glass (which only had one ARM experiment and one IRM experiment) to reduce uncertainties associated with sample orientation ($\pm 5^\circ$). The nature of the anisotropy of remanence in each sample can be characterized by two parameters: the degree of anisotropy, P , and the shape factor, T . P is defined as the ratio of the magnetic moments acquired along the easy axis and hard axes of the anisotropy ellipsoid. T is calculated from relative ratios of moments acquired along the easy, medium, and hard axes, and provides information regarding the shape of the anisotropy ellipsoid. Positive values of T indicate oblate ellipsoids, while negative values indicate prolate ellipsoids.

We found that sample 15556,221c, which exhibited zig-zag demagnetization, is by far our most strongly anisotropic sample and has an oblate fabric ($P=2.0$, $T=0.17$ for ARM; $P=2.6$, $T=0.30$ for IRM) and a well-defined easy plane (i.e., plane defined by the easy and intermediate magnetic axes). The two antipodal pinned directions lie within 22.5° from the easy axis of magnetization and within 18° of the easy plane (Fig. 7). We estimate that the uncertainty of this easy plane orientation to be $<3^\circ$, based on the differences in the location of the pole of the easy plane (hard axis direction) between experiments. The MAD values derived from PCA fits for each of the two directional groups are 27.7° and 31.6° . Since the angular distances between the pinned magnetization

directions and the easy plane are less than the MADs of the PCA fits, the magnetization directions essentially fall within error of the easy plane. This demonstrates that pinning during AF demagnetization is very likely due to the high magnetic anisotropy of this subsample. Similar but preliminary observations using susceptibility anisotropy were reported for several lunar samples with spurious remanence by Brecher (1977).

Anisotropy alone cannot explain why the moment of 15556,221c flips back and forth in the easy plane as opposed to being stably oriented in one direction. As discussed above (Sections 3 and 4), 15556 is highly susceptible to acquisition of spurious ARM during AF demagnetization. We propose that spurious ARM is also responsible for the flipping observed for 15556,221c. To test this hypothesis, we repeated AF applications multiple times for each applied field level during demagnetization of NRM (as described in Section 3.1). We counted how many times the magnetic moment flipped between antipodal directions for each AF level and determined the fraction of AF applications which led to flips. In general, the flipping frequency increased with AF level up to 10 mT before leveling off at a 50% chance of flipping at any given AF application (see Supplementary material and Fig. S12). This increase suggests that ARM noise is the causative factor because the net moment becomes increasingly dominated by spurious ARM at progressively higher AF steps. If flipping was solely controlled by an unbiased AC field with random thermal fluctuations, one would expect the 50% flipping frequency to start at the first flip at the AF level of the first flip (3 mT). This likely explains similar pinning and zig-zag demagnetization observed in other lunar samples (Brecher, 1976; Hoffman and Banerjee, 1975).

We found that the other subsamples of 15556 were less anisotropic than 15556,221c, with P values ranging from 1.13–1.52. Subsamples of 12017 and 15016 had similar values with average $P=1.14$ and 1.55, respectively (Tables S8 and S9). 10020,234b4 and 10020,234d had average P ranging from 1.12–1.73, respectively [see Shea et al. (2012)]. Our anisotropy results, in conjunction with other remanence anisotropy parameters previously published for lunar rocks by Cournede et al. (2012) and Potter (2011), indicate an inverse correlation between P and sample size (Fig. 8). This likely indicates that the anisotropy is a

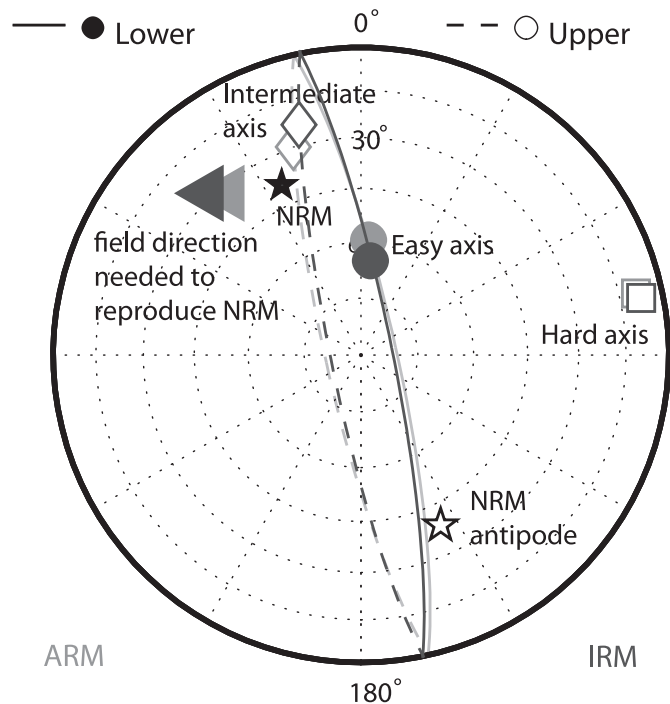


Fig. 7. Equal area stereographic projection of anisotropy of remanence results for sample 15556,221c. Open symbols and dashed lines represent points and portions of great circles in the upper hemisphere. Closed symbols and solid lines represent points and portions of great circles in the lower hemisphere. Stars represent the NRM direction and its antipode. Circles, diamonds, and squares represent the easy, medium, and hard directions of the remanence anisotropy ellipsoids, respectively. Light gray symbols represent results from the ARM experiment, while dark gray symbols represent those from the IRM experiment.

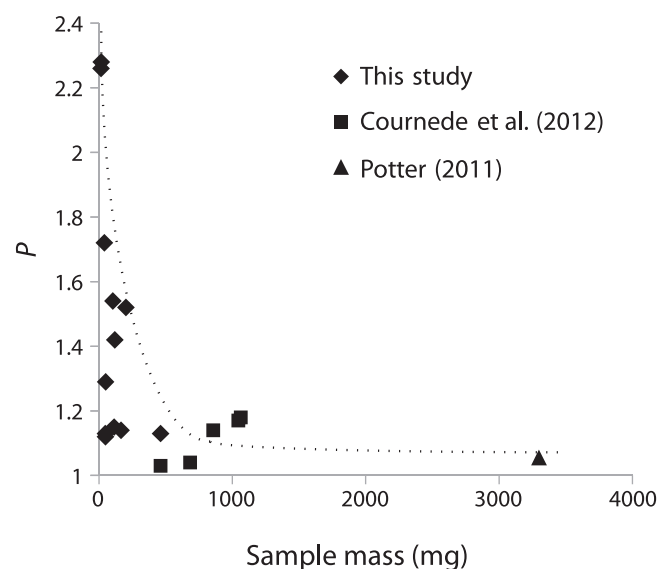


Fig. 8. Degree of anisotropy (P) vs. mass of all samples subjected to anisotropy of remanence experiments in this study. Dashed line highlights trend in data. Anisotropy results from this study are represented by diamonds, while those from Cournede et al. (2012) and Potter (2011) are represented by squares and triangles, respectively.

reflection of a small number of metal grains with shape anisotropy which are likely to dominate samples with small masses.

6. Discussion

The unbrecciated, unshocked, primary igneous textures of basalts 15556, 15016, and 12017 would at first glance appear to make them ideal candidates for lunar paleomagnetism studies. However, like many other lunar samples reported in the literature (Table S1), these samples behave unstably during AF demagnetization experiments and are poor recorders of magnetic fields of strengths predicted for an ancient lunar dynamo. Their NRM does not decline monotonically toward the origin with application of increasing peak AF fields. There is a large amount of scatter in both magnitude and direction of remanent magnetization at AF fields above 20 mT. This is a clear demonstration of the deleterious effects of spurious ARM acquired during AF demagnetization. As discussed in the Supplementary material, scatter in moment magnitude and direction resulting from acquisition of spurious ARM may cause noisy HC magnetization directions to appear origin-trending (i.e. primary) in the dANG/MAD test when they may or may not actually be. Alternatively, ARM noise may obscure an otherwise origin-trending magnetization, further complicating the task of determining whether the magnetizations of low-fidelity lunar samples can be primary TRM. One subsample, 15556,221c, exhibited anisotropy-controlled pinning behavior, with the magnetization direction flipping between two antipodal directions without decaying in intensity. None of our basalt samples acquired significant GRM, although it has previously been shown that GRM significantly affects 76535 (Garrick-Bethell et al., 2009).

Our hysteresis and rock magnetic studies show that mare basalts 15556, 15016, and 12017 possess a higher fraction of multidomain kamacite than samples which express stable AF demagnetization such as 10020, the 12017 glass, and 76535. As explained in Section 1, samples dominated by multidomain magnetic carriers possess lower coercivities and are more susceptible to spurious ARM noise. This explains why some subsamples are almost completely demagnetized at low AF amplitudes (below 20 mT). The greater susceptibility to GRM acquisition of 76535 likely relates to the relative finer grain size of its ferromagnetic minerals relative to the other samples in this study.

Spurious ARM noise also affects IRM and ARM paleointensity studies, which rely on AF demagnetization as part of the paleointensity method. This effect means that most samples with unstable AF demagnetization will not provide accurate AF-based paleointensities for paleofields weaker than a certain threshold value. We observe a threshold of $\sim 37 \mu\text{T}$ for two of the basalt subsamples analyzed during this study. This value is above the theoretical estimates of the maximum lunar surface field that could be generated by a small lunar core Dwyer et al., 2011; Le Bars et al., (2011); Wieczorek et al., 2006). Therefore, many lunar rocks are not suitable for AF-based paleointensity studies of expected lunar field intensities. This conclusion has major implications for our current understanding of the lifetime of the lunar dynamo that has been inferred from REMc paleointensities. In particular, spurious ARM may also be responsible for the minimum $\sim 1 \mu\text{T}$ paleofield consistently estimated for samples younger than the expected lifetime of an ancient lunar dynamo [see Fig. 3.22 of Wieczorek et al. (2006)].

For samples susceptible to spurious ARM, better demagnetization and paleointensity techniques are necessary. If thermal demagnetization and Thellier–Thellier techniques can be developed so as to avoid alteration, they could be powerful tools for

understanding the true nature of lunar remanent magnetization. Experiments on terrestrial rocks have successfully retrieved paleofields as low as $1 \mu\text{T}$ (Tanaka and Kono, 1984). These results demonstrate that thermal-based techniques are in principle capable of recovering the weak ($< 15\text{--}20 \mu\text{T}$) fields expected for the lunar dynamo. Using the Thellier–Thellier technique, Lawrence et al. (2008) were able to successfully recover paleointensities of just $5 \mu\text{T}$ from laboratory TRMs for three lunar samples, two of which were demonstrably multidomain (Lawrence and Johnson, 2009) (with the important caveat that at least two of these samples had been altered during previous thermal demagnetization experiments). However, even if thermal methods could be perfected to entirely avoid alteration, AF methods may still be required to remove low coercivity overprints. Therefore, the development of low-ARM noise AF systems may be a preferable alternative for future lunar paleomagnetic studies.

As described in Section 5, we observed a correlation between sample size and degree of anisotropy P . A similar correlation was previously observed in anisotropy of magnetic susceptibility (AMS) studies on the Knyahinya L/LL5 chondrite by Gattacceca et al. (2005). Larger samples have the advantage of having more ferromagnetic grains that contribute to the magnetization, which tempers the effects of magnetic anisotropy from individual grains. Therefore, it may be beneficial to conduct paleomagnetic analyses on larger subsamples. Our experiments on lunar basalts (Fig. 8) suggest that a minimum sample size for mare basalts should be $\sim 150 \text{ mg}$.

7. Conclusions

- Unstable AF demagnetization behavior, observed in some lunar samples as well as meteorites, often makes it difficult to determine whether ancient magnetic fields existed on their parent bodies.
- Multidomain samples often have poor demagnetization behavior and yield unreliable absolute paleointensities using AF-based methods. This is a particular problem for extraterrestrial paleomagnetism because of the predominance of multidomain carriers and the more widespread use of AF demagnetization relative to Earth paleomagnetism.
- Spurious ARM noise and magnetic anisotropy can explain unstable AF demagnetization and pinning in extraterrestrial samples.
- GRM acquisition is likely a problem of secondary importance since it was only observed in one of the samples considered here. This is likely due to the dominant multidomain grain sizes of the samples.
- Better techniques need to be developed to study samples susceptible to spurious ARM. Possibilities include low-noise AF systems and thermal demagnetization and Thellier–Thellier methods that avoid sample alteration.
- Spurious ARM may be responsible for $\geq 1 \mu\text{T}$ paleointensities previously computed for samples likely to postdate a lunar dynamo.
- Unless a sample can be shown to preserve stable low-field laboratory induced TRM or ARM, unstable AF demagnetization of does not provide evidence against the presence of an ancient lunar dynamo.

Acknowledgments

We thank CAPTEM for allocating the samples and the staff of the NASA Lunar Sample Laboratory for assistance in sample preparation and acquisition. We also thank F. Demory of CEREGE

and J. Bowles at the Institute of Rock Magnetism for assistance in acquiring hysteresis and FORC measurements, N. Chatterjee for assisting with microprobe measurements, R. Fu with developing methods for accurate low bias field ARM acquisition, and C. Ross for use of her vibrating sample magnetometer. SMT and EKS were supported by a NASA Earth and Space Science Fellowship. SMT was supported by a National Science Foundation Graduate Research Fellowship and the NASA Lunar Science Institute. This work was also supported by grants from the NASA Lunar Advanced Science and Exploration Research Programs to BPW and the NASA Lunar Science Institute to BPW and TLG.

Appendix A. Supporting information

Supplementary data associated with this article can be found in the online version at <http://dx.doi.org/10.1016/j.epsl.2012.05.024>.

References

- Acton, G., Yin, Q.Z., Verosub, K.L., Jovane, L., Roth, A., Jacobsen, B., Ebel, D.S., 2007. Micromagnetic coercivity distributions and interactions in chondrules with implications for paleointensities of the early solar system. *J. Geophys. Res.*, 112, <http://dx.doi.org/10.1029/2006JB004655>.
- Brecher, A., 1976. Textural remanence: a new model of lunar rock magnetism. *Earth Planet. Sci. Lett.* 29, 131–145.
- Brecher, A., 1977. Interrelationships between magnetization directions, magnetic fabric, and oriented petrographic features in lunar rocks. In: *Proceedings of the 8th Lunar Science Conference*, pp. 703–723.
- Brecher, A., Leung, L., 1979. Ancient magnetic field determinations on selected chondritic meteorites. *Phys. Earth Planet. Inter.* 20, 361–378.
- Cisowski, S., Collinson, D., Runcorn, S., Stephenson, A., Fuller, M., 1983. A review of lunar paleointensity data and implications for the origin of lunar magnetism. In: *Proceedings of the 13th Lunar Planetary Science Conference*, pp. A691–A704.
- Collinson, D., 1983. *Methods in Rock Magnetism and Paleomagnetism*. Chapman and Hall, New York, NY.
- Cournede, C., Gattacceca, J., Rochette, P., 2012. Magnetic study of large Apollo samples: possible evidence for an ancient centered dipolar field on the Moon. *Earth Planet. Sci. Lett.* 331–332, 31–42.
- Dunlop, D., Ozdemir, O., 1997. *Rock Magnetism: Fundamentals and Frontiers*. Cambridge, UK.
- Dunlop, D.J., 2002a. Theory and application of the Day plot (Mrs/Ms versus Hcr/Hc) - 2. Application to data for rocks, sediments, and soils. *J. Geophys. Res.*, 107, <http://dx.doi.org/10.1029/2001JB000487>.
- Dunlop, D.J., 2002b. Theory and application of the Day plot (Mrs/Ms versus Hcr/Hc) - 1. Theoretical curves and tests using titanomagnetite data. *J. Geophys. Res.*, 107, <http://dx.doi.org/10.1029/2001JB000486>.
- Dwyer, C., Stevenson, D., Nimmo, F., 2011. A long-lived lunar dynamo driven by continuous mechanical stirring. *Nature* 479, 212–214.
- Dyal, P., Parkin, C., Sonett, C., 1970. Apollo 12 Magnetometer: measurement of a steady magnetic field on the surface of the Moon. *Science* 169, 762–764.
- Evensen, N., Murthy, V., Coscio, M., 1973. Rb-Sr ages of some mare basalts and the isotopic and trace element systematics in lunar fines. In: *Proceedings of the 4th Lunar Science Conference*, 1707–1724.
- Fleischer, R., Hart, H., Comstock, G., Ewvaraye, A., 1971. The particle track record of the ocean of storms. In: *Proceedings of the 2nd Lunar Science Conference*, pp. 2559–2568.
- Fuller, M., Cisowski, S., 1987. Lunar paleomagnetism. *Geomagnetism* 2, 307–455.
- Garcia, R., Gagnepain-Beyneix, J., Chevrot, S., Lognonne, P., 2010. The lunar core revealed by reflected seismic waves: constraints on the deep Moon seismic structure. *EOS Transactions. AGU Fall Meeting, Abs. #P43B*.
- Garrick-Bethell, I., Weiss, B., Shuster, D., Buz, J., 2009. Early lunar magnetism. *Science* 323, 356–359.
- Garrick-Bethell, I., Weiss, B., Gattacceca, J., 2010. Pressure magnetization experiments and a common magnetization direction in mutually oriented samples of lunar troctolite 76535. In: *Proceedings of the 73rd Annual Meteorological Society Meeting* 5395.
- Gattacceca, J., Rochette, P., Denise, M., Consolmagno, G., Folco, L., 2005. An impact origin for the foliation of chondrites. *Earth Planet. Sci. Lett.* 234, 351–368.
- Gattacceca, J., Berthe, L., Boustie, M., Vadeboin, F., Rochette, P., De Resseguier, T., 2008. On the efficiency of shock magnetization processes. *Phys. Earth. Planet. Inter.* 166, 1–10.
- Gattacceca, J., Boustie, M., Hood, L., Cuq-Lelandais, J.-P., Fuller, M., Bezaeva, N., de Resseguier, T., Berthe, L., 2010. Can the lunar crust be magnetized by shock: experimental groundtruth. *Earth Planet. Sci. Lett.* 299, 42–53.
- Geiss, J., Eberhardt, P., Grogler, N., Guggisberg, S., Maurer, P., Stettler, A., 1977. Absolute time scale of lunar mare formation and filling. *Philos. Trans. R. Soc. A* 285, 151–158.
- Guggisberg, S., Eberhardt, P., Geiss, J., Grogler, N., Stettler, A., 1979. Classification of the Apollo-11 mare basalts according to Ar39-Ar40 ages and petrological properties. In: *Proceedings of the 10th Lunar Planetary Science Conference*, pp. 1–39.
- Hoffman, K., Banerjee, S., 1975. Magnetic “zig-zag” behavior in lunar rocks. *Earth Planet. Sci. Lett.* 25, 331–337.
- Hood, L., Mitchell, D., Lin, R., Acuna, M., Binder, A., 1999. Initial measurements of the lunar induced magnetic dipole moment using Lunar Prospector magnetometer data. *Geophys. Res. Lett.* 26, 2327–2330.
- Hood, L., Artemieva, N., 2008. Antipodal effects of lunar basin-forming impacts: initial 3D simulations and comparisons with observations. *Icarus* 193, 485–502.
- Horn, P., Kirsten, T., Jessberger, E., 1975. Are there A 12 mare basalts younger than 3.1 b.y. Unsuccessful search for A 12 mare basalts with crystallization ages below 3.1 b.y. *Meteoritics* 10, 417–418.
- Hu, S., Appel, E., Hoffmann, V., Schmahl, W.W., Wang, S., 1998. Gyromagnetic remanence acquired by greigite (Fe₃S₄) during static three-axis alternating field demagnetization. *Geophys. J. Int.* 134, 831–842.
- Kirschvink, J., 1980. The least-squares line and plane and the analysis of palaeomagnetic data. *Geophys. J. R. Astr. S* 62, 699–718.
- Kirschvink, J., Kopp, R., Raub, T., Baumgartner, C., Holt, J., 2008. Rapid, precise, and high-sensitivity acquisition of paleomagnetic and rock magnetic data: development of a low-noise automatic sample changing system for superconducting rock magnetometers. *Geochim. Geophys. Geosyst.* 9, 1–18.
- Kirsten, T., Deubner, J., Horn, P., Kaneoka, I., Kiko, J., Schaeffer, O., Thio, S., 1972. The rare gas record of Apollo 14 and 15 samples. In: *Proceedings of the 3rd Lunar Planetary Science Conference*, pp. 1865–1889.
- Konopliv, A., Binder, A., Hood, L., Kucinskis, A., Sjogren, W., Williams, J., 1998. Improved gravity field of the Moon from Lunar Prospector. *Science* 281, 1476–1480.
- Kramer, F.E., Twedell, D.B., Walton, W.J.A., 1977. Apollo 11 Lunar Sample Information Catalogue. Nat. Aeronaut. Space Adm., Houston, TX.
- Lawrence, K., Johnson, C., Tauxe, L., Gee, J., 2008. Lunar paleointensity measurements: implications for lunar magnetic evolution. *Phys. Earth Planet. Inter.* 168, 71–87.
- Lawrence, K., Johnson, C., 2009. Magnetic characterization of lunar samples: back to basics. In: *Proceedings of the 40th Lunar Planetary Science*, p. 1433.
- Le Bars, M., Wiczeorek, M., Karatekin, O., Cebron, D., Laneuville, M., 2011. An impact-driven dynamo for the early Moon. *Nature* 479, 215–218.
- Meyer, C., 2008. The Lunar Sample Compendium (online). <<http://www-curator.jsc.nasa.gov/lunar/compendium.cfm>>.
- Morrison, D.M., D.S., Heiken, G., Moore, H., 1973. Microcraters on lunar rocks. In: *Proceedings of the 3rd Lunar Science Conference*, pp. 2767–2791.
- Nagata, T., Fisher, R., Schwerer, F., Fuller, M., Dunn, J., 1972. Summary of Rock Magnetism of Apollo 15 Lunar Materials. The Apollo 15 Lunar Samples. The Lunar Science Institute, Houston, pp. 442–445.
- Nagata, T., Fisher, R., Schwerer, F., Fuller, M., Dunn, J., 1973. Magnetic properties and natural remanent magnetization of Apollo 15 and 16 lunar materials. In: *Proceedings of the 4th Lunar Science Conference*, pp. 3019–3043.
- Pearce, G., Gose, W., Strangway, D., 1973. Magnetic studies on Apollo 15 and 16 lunar samples. In: *Proceedings of the 4th Lunar Science Conference*, pp. 3045–3076.
- Pike, C., Roberts, A., Verosub, K., 1999. Characterizing interactions in fine magnetic particle systems using first order reversal curves. *J. Appl. Phys.* 85, 6660–6667.
- Potter, D., 2011. Novel magnetic techniques for rapidly detecting palaeomagnetically important single-domain iron particles and obtaining directional palaeomagnetic data from “unoriented” lunar rock samples. *Can. Aeronaut. Space J.* 57, 12–23.
- Pritchard, M., Stevenson, D., 2000. Thermal aspects of a lunar origin by giant impact. In: Canup, R., Righter, K. (Eds.), *Origin of the Earth and Moon*. University of Arizona Press, Tucson, pp. 179–196.
- Runcorn, S.K., 1996. The formation of the lunar core. *Geochim. Cosmochim. Acta* 60, 1205–1208.
- Shea, E., Weiss, B., Cassatta, W., Shuster, D., Tikoo, S., Gattacceca, J., Grove, T., Fuller, M., 2012. A long-lived lunar core dynamo. *Science* 335, 453–456.
- Srnka, L., 1977. Spontaneous magnetic field generation in hypervelocity impacts. In: *Proceedings of the 8th Lunar Planetary Science Conference*, pp. 785–792.
- Stegman, D., Jellinek, A., Zatman, S., Baumgardner, J., Richards, M., 2003. An early lunar dynamo driven by thermochemical mantle convection. *Nature* 421, 143–146.
- Stephenson, A., Collinson, D., 1974. Lunar magnetic field paleointensities determined by an anhysteretic remanent magnetization method. *Earth Planet. Sci. Lett.* 23, 220–228.
- Stephenson, A., 1980. A gyroremanent magnetisation in anisotropic magnetic material. *Nature* 284, 49–51.
- Stephenson, A., Sadikun, S., Potter, D., 1986. A theoretical and experimental comparison of the anisotropies of magnetic susceptibility and remanence in rocks and minerals. *Geophys. J. R. Astron. Soc.* 84, 185–200.
- Stephenson, A., 1993. Three-axis static alternating field demagnetization of rocks and the identification of natural remanent magnetization, gyroremanent magnetization, and anisotropy. *J. Geophys. Res.* 98, 373–381.

- Tanaka, H., Kono, M., 1984. Analysis of the Thelliers' method of paleointensity determination 2: Applicability to high and low magnetic fields. *J. Geomagn. Geoelectr.* 36, 285–297.
- Warner, J., 1970. Apollo 12 Lunar Sample Information Catalog. Nat. Aeronaut. Space Adm., Washington, DC.
- Weber, R., Lin, P., Garnero, E., Williams, Q., Lognonne, P., 2011. Seismic detection of the lunar core. *Science* 331, 309–312.
- Weiss, B., Gattacceca, J., Stanley, S., Rochette, P., Christensen, U., 2010. Paleomagnetic records of meteorites and early planetesimal differentiation. *Space Sci. Rev.* 152, 341–390.
- Wieczorek, M., Jolliff, B., Khan, A., Pritchard, M., Weiss, B., 2006. The constitution and structure of the lunar interior. *Rev. Mineral. Geochem.* 60, 221–364.
- Wieczorek, M., Weiss, B., Stewart, S., 2012. An impactor origin for lunar magnetic anomalies. *Science* 335, 1212–1215.

**Supplementary Material for:
Magnetic Fidelity of Lunar Samples and Implications for an Ancient Core Dynamo**

Sonia M. Tikoo, Benjamin P. Weiss, Jennifer Buz, Eduardo A. Lima, Erin K. Shea, Gabriela Melo, Timothy L. Grove

1. Introduction

1.1. Nonideal AF demagnetization behavior of extraterrestrial samples. For a rock to provide compelling evidence that it acquired its magnetization during cooling through a stable magnetic field, its characteristic remanent magnetization component must linearly and continuously decline toward the origin during stepwise demagnetization by either alternating fields (AF) or thermal methods. As discussed in the main text, a frequent impediment to extraterrestrial

Table S1. Lunar rocks and meteorites reported to have nonideal AF demagnetization behavior.

Sample	Behavior	Reference
Lunar Samples		
12002	NM, S	Strangway et al. (1971)
12017*	NM, S	Strangway et al. (1971)
12051	NM, S	Strangway et al. (1971)
12063	NM, S	Strangway et al. (1971)
15016*	S	Pearce et al. (1973)
15076	NM, S	Pearce et al. (1973)
15085	NM	Collinson et al. (1972)
15086	NM	Collinson et al. (1972)
15415	NM, S	Pearce et al. (1973)
15499	NM, S	Fuller et al. (1979)
15535	NM, ZZP	Hoffman and Banerjee (1975)
15555	NM	Cisowski et al. (1977)
15556*	NM, S	Cisowski et al. (1977), Nagata et al. (1973), Gattacceca et al. (2010), Cournede et al. (2012)
67016	NM, S	Pearce et al. (1973)
60335	NM, S	Pearce et al. (1973)
Meteorites		
<i>Ordinary chondrites</i>	NM, S	Morden and Collinson (1992)
<i>EET 87503</i>	NM, S	Collinson and Morden (1994)
<i>Kapoeta</i>	NM	Collinson and Morden (1994)
<i>Petersburg</i>	NM, S	Collinson and Morden (1994)
<i>Bensour</i>	NM, ZZP	Gattacceca et al. (2003)

Note: The first column contains sample names. The second column describes the nature of the reported AF demagnetization behavior. NM = non-monotonic decline of moment; S = scatter in magnetization direction; ZZP = zig-zag demagnetization and pinning of magnetization to an anisotropic easy plane. The third column lists the sources reporting paleomagnetic data for the respective samples. Asterisks (*) denote samples measured in this study.

paleomagnetic studies is the presence of unstable AF demagnetization behavior, manifested as non-monotonic decline of magnetic moment, scatter in magnetization directions, and sometimes pinning of magnetization to an axis or plane (Table S1). These behaviors make it difficult to infer the origin of any paleofield recorded in such samples.

We posit that spurious anhysteretic remanence (ARM) and gyroremanent magnetization (GRM) are possible sources for unstable demagnetization behavior. We further discuss, and essentially rule out, substantial GRM acquisition for all of our measured samples except for 76535 (see Section 5.2 of this document). Spurious ARM may be produced by the presence of phase-shifted even harmonics or other unwanted frequencies which may appear in the AF waveform during demagnetization experiments.

In the main text, we showed how a phase-shifted even harmonic can produce a biasing remanence in samples during demagnetization (Fig. 1a). Ideally, the AF waveform should consist of just the fundamental component, which is a perfect sinusoidal waveform centered about zero. The amplitude of this component is then modulated to create ramp-up, steady, and ramp-down segments. In practice, nonlinearities in electronic circuits and components create harmonics in the basic AF waveform. Phase-shifted even harmonics are particularly troublesome, as they often create an asymmetry in positive and negative peak values of the AF signal, which effectively corresponds to imparting an ARM (Fig. S1).

Note, however, that no DC bias is actually created by adding harmonics to a fundamental component, regardless of the relative amplitude ratios and phase shifts of the components. The average value of the resulting waveform is always zero because each component is centered about zero (Fig. S1a). However, whenever the odd symmetry (i.e., antisymmetry about the vertical axis) of the resulting waveform is broken—which only happens when out-of-phase even harmonics are added (Fig. S1b,c)—the net effect on a sample is similar to applying a DC field together with a sinusoidal field.

Fig. S1a shows an example of an AF waveform comprised of a fundamental component combined with an in-phase second harmonic. In this case, because the odd symmetry of the waveform is preserved, the effect of adding a second harmonic is to evenly increase the amplitude of the peaks in the AF signal. Although the resulting waveform no longer looks like a sinusoid, the positive and negative peaks are still symmetric, albeit larger. The quantities $\Delta 1$ and $\Delta 2$ indicated in Figs. S1a-c represent, respectively, the increase in magnitude of the positive and negative peaks of the resulting waveform with respect to the fundamental.

If we shift the second harmonic by 45° with respect to the fundamental, we get the waveform shown in Fig. S1b. Here, we can see that the positive peak increases while the negative one decreases and the resulting waveform no longer displays odd symmetry. Further shifting the second harmonic so that it is 90° out of phase with respect to the fundamental yields the waveform shown in Fig S1c, in which the positive peak increases by the same amount the negative peak decreases (provided the amplitude of the second harmonic is less than or equal to one quarter of the amplitude of the fundamental). The effective bias fields for the three different cases are shown below (note that negative $\Delta 1$ or $\Delta 2$ quantities indicate a decrease in respective peak magnitudes):

- **Case 1** (Fig. S1a): $\Delta 1 = \Delta 2 = \Delta > 0$; effective bias field = 0 (no ARM imparted) ;
- **Case 2** (Fig. S1b): $\Delta 1 > 0$, $\Delta 2 < 0$, $|\Delta 1| > |\Delta 2|$; effective bias field = $(|\Delta 1| + |\Delta 2|)/2$;
- **Case 3** (Fig. S1c): $\Delta 1 = -\Delta 2 = \Delta > 0$; effective bias field = Δ .

The relative amplitude and phase shift of the harmonics are approximately fixed for most AF amplitudes, with exception of those nearing the maximum absolute amplitude supplied by the instrument. This means that, in general, $\Delta 1$ and $\Delta 2$ are proportional to the amplitude of the fundamental. Thus, during the ramp-down segment, a different effective ARM bias field is applied at each cycle of the AF waveform, which makes high-coercivity grains experience a larger bias field than low-coercivity ones. This, in fact, does not correspond to a single ARM application; instead, it is equivalent to a sequence of ARM applications with decreasing maximum AF and bias fields.

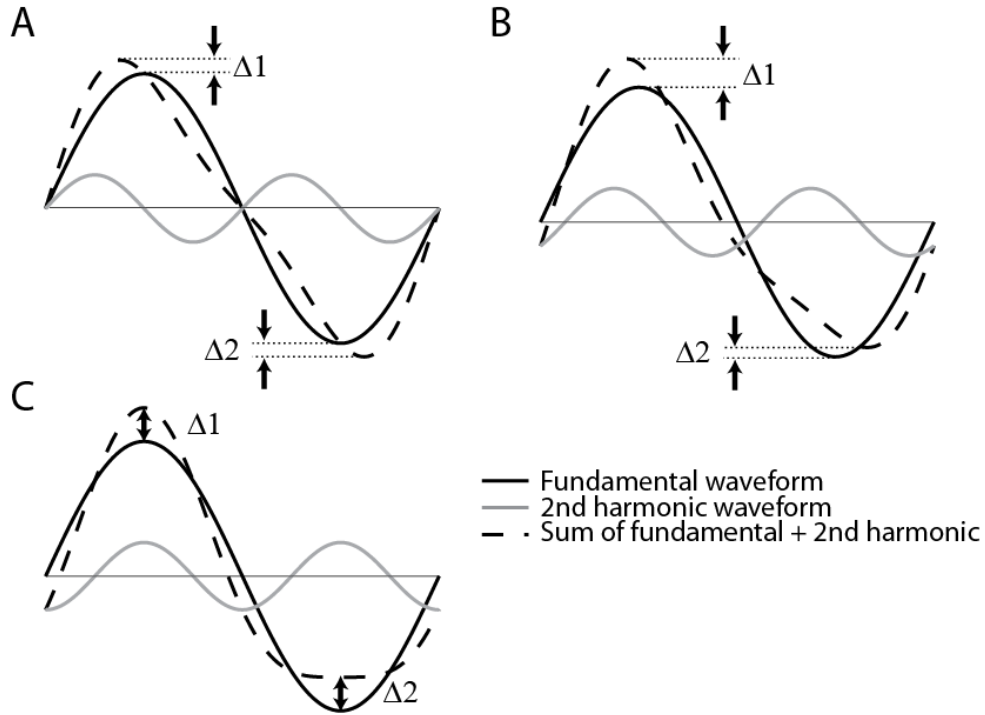


Figure S1. Generation of spurious ARM as a result of the summation of the fundamental AF waveform component with second harmonics at different phases. $\Delta 1$ represents the increase in magnitude of the positive peak, whereas $\Delta 2$ represents the increase in magnitude of the negative peak. (A) Second harmonic is in phase with the fundamental. (B) Second harmonic is phase shifted by 45° with respect to the fundamental. (C) Second harmonic is phase shifted by 90° with respect to the fundamental (this is the same case as depicted in Fig. 1). Modified from Collinson (1983).

To characterize the harmonic content in our AF applications, we utilized a pick-up coil placed in the AF coil set region and a digital oscilloscope to measure the frequency spectrum of the voltage induced in this test coil. Below, we show that harmonic frequencies are present and contaminate the principal AF waveform experienced by the sample (Fig. S2). In addition, non-harmonic waveforms are occasionally present (e.g., those with frequencies of 1086 Hz, 3349 Hz, and 4827 Hz in Fig. S2a), which may also introduce spurious magnetizations to a sample as their amplitudes are similar to that of the second harmonic. It is unclear if these non-harmonic components are produced by the AF system or whether they come from some other source in the laboratory. (Regardless of their origin, such fields are present in the region where the sample is demagnetized, thus affecting the results of AF applications.) Whereas the AF waveform itself (fundamental and harmonics) seems very consistent, we observed that the overall spectral characteristics often change, particularly the noise floor and the presence of stronger non-

harmonic waveforms. Such components are especially pernicious, given that they yield unpredictable changes in AF peak asymmetry and may further increase the noise associated with higher demagnetization steps.

1.2. Samples analyzed in this study. We studied the AF demagnetization and magnetic fidelity of five lunar rocks to further investigate sources of noisy demagnetization and resulting implications for extraterrestrial paleomagnetic studies. Subsamples from lunar rocks 15556, 15016, and 12017 were chipped from their respective parent rocks at the NASA Lunar Receiving Laboratory at Johnson Space Center. The majority of sample handling took place within a class ~10,000 clean laboratory located within a magnetically shielded room (magnetic field < 200 nT) at the MIT Paleomagnetism Laboratory (<http://web.mit.edu/paleomag>). The samples were stored within this magnetically shielded room for between 1-24 months (depending on subsample) prior to commencing magnetic experiments. We conducted numerous experiments on these samples including AF demagnetization of the natural remanent magnetization (NRM), paleointensity determinations, magnetic hysteresis, and additional rock magnetic characterization experiments. We compared results from our studies of 15556, 15016, and 12017 to those of the high-fidelity samples 10020 and 76535 conducted by Shea et al. (2012) and Garrick-Bethell et al. (2009), respectively. In this supplement, we provide further details regarding these investigations and their results.

2. Petrographic Analyses

2.1. Cooling rates and implications for magnetization. A key way to establish that the characteristic remanent magnetization in a lunar sample is a thermoremanent magnetization (TRM) acquired in a stable, long-lived field like that expected from a dynamo is to demonstrate that the timescale for late-stage cooling is much longer than the duration of postulated impact fields (maximum ~ 1 day for the largest, basin-forming impacts) (Crawford and Schultz, 1999; Hood and Artemieva, 2008). This is because if a sample cools slowly, a transient field could only impart magnetization to magnetic carriers within a narrow range of blocking temperatures, such that most blocking temperature and coercivity fractions will appear unmagnetized during demagnetization experiments.

Cooling rate studies of quartz-normative mare basalts have established that the width of plagioclase laths and the nucleation density of pyroxene phenocrysts each directly correlate with the late-stage (starting at 1120°C) cooling rate (Grove and Walker, 1977). Therefore, to determine the cooling rates of our samples, we measured the width of the [010] face (perpendicular to albite twinning) of the largest pristine plagioclase laths in 15556, 15016, 12017, and 10020 (see Fig. S3). While 15556 and 15016 are not quartz-normative, their liquidus temperatures for plagioclase are close to those of the quartz-normative basalts used in Grove and Walker (1977), so use of the plagioclase width technique is likely still valid (Humphries et al., 1972). The measured plagioclase widths for 15556 and 15016 correspond to late-stage cooling

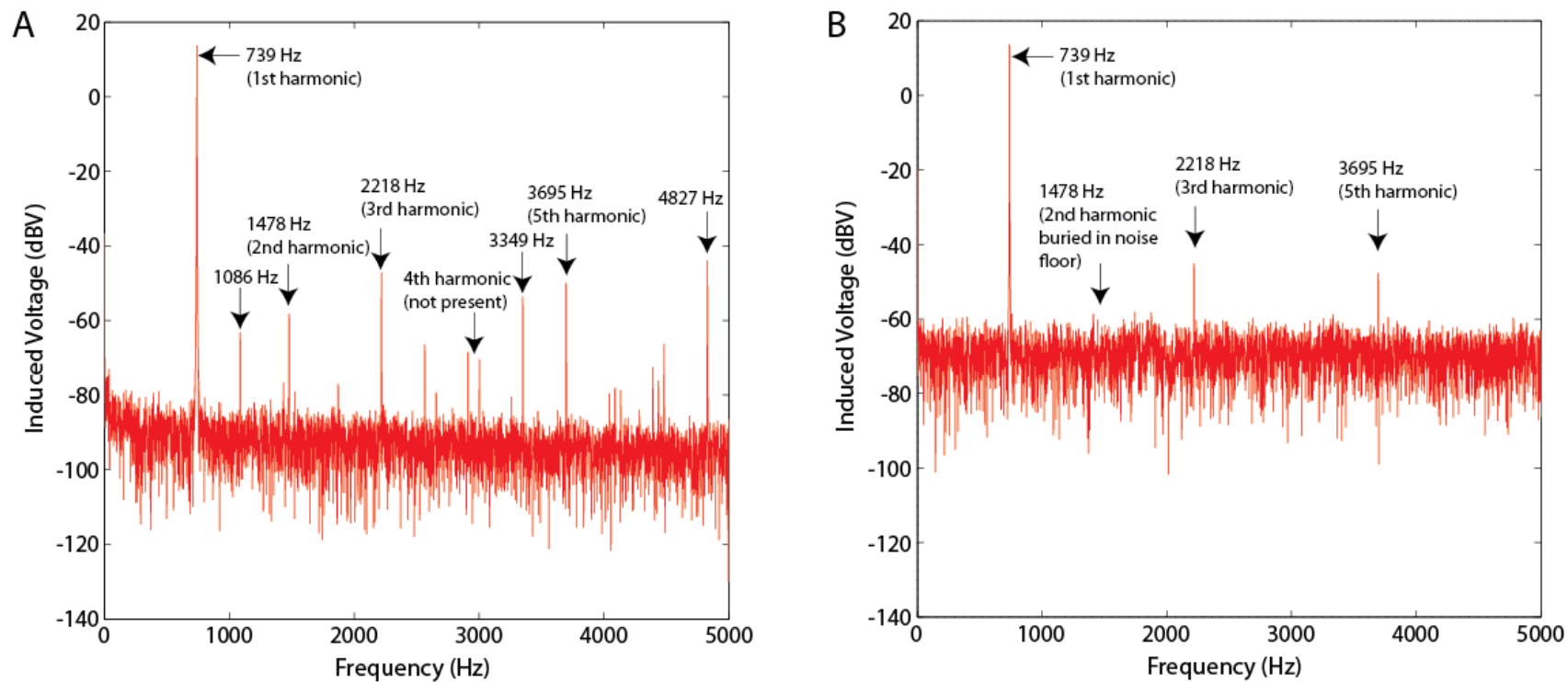


Figure S2. Frequency spectra of typical AF applications in the MIT Paleomagnetism Laboratory system measured on different days (A) Day 1. (B) Day 2. Shown is induced voltage [in decibel volts (dBV)] vs. frequency (in Hz) during an AF application to a peak AC field of 20 mT. Data were measured using a pick-up coil placed in the AF coil region and connected to a digital oscilloscope. Peaks represent waveforms present during AF application and are annotated if they are the result of harmonic frequencies or additional spurious frequencies with comparable magnitude.

rates of 0.3°C/hour and 0.6°C/hour, respectively. Sample 12017 is quartz normative (Rhodes et al., 1977). Using both plagioclase widths and pyroxene nucleation density, we determined the cooling rate of the 12017 basalt to be 0.4°C/hour. For 10020, Shea et al. (2012) used measurements of plagioclase widths to infer exactly the same cooling rate of 3°C/hour previously reported by Beaty and Albee (1978). While 10020 is not quartz normative and is low-Ti, Beaty and Albee (1978) suggested that their cooling rate estimate for this sample is robust because their cooling rate results for numerous low-Ti Apollo 11 samples were similar to cooling rate estimates from high-Ti samples using an independent method in Usselman et al. (1975). Assuming cooling rate remains constant at subsolidus temperatures, these results suggest that basalts 15556, 15016, 12017, and 10020 cooled from the Curie point of iron (~780°C) to ambient surface temperatures (~-170°C to 100°C) over periods of hours to months. Troctolite 76535, studied by Garrick-Bethell et al. (2009), cooled over a timescale of thousands to millions of years. Therefore, any TRM in all five of these samples is very unlikely to be the result of an impact-generated magnetic field. Furthermore, the lack of observed shock effects indicates that shock remanent magnetization (SRM) components or shock demagnetization effects must be modest.

We do not see any correlation between the inferred cooling rate and the fidelity of magnetization during AF demagnetization. In particular, we found that 15556, 15016 and 12017 do not possess high fidelity AF demagnetization records and hence cannot readily be used to

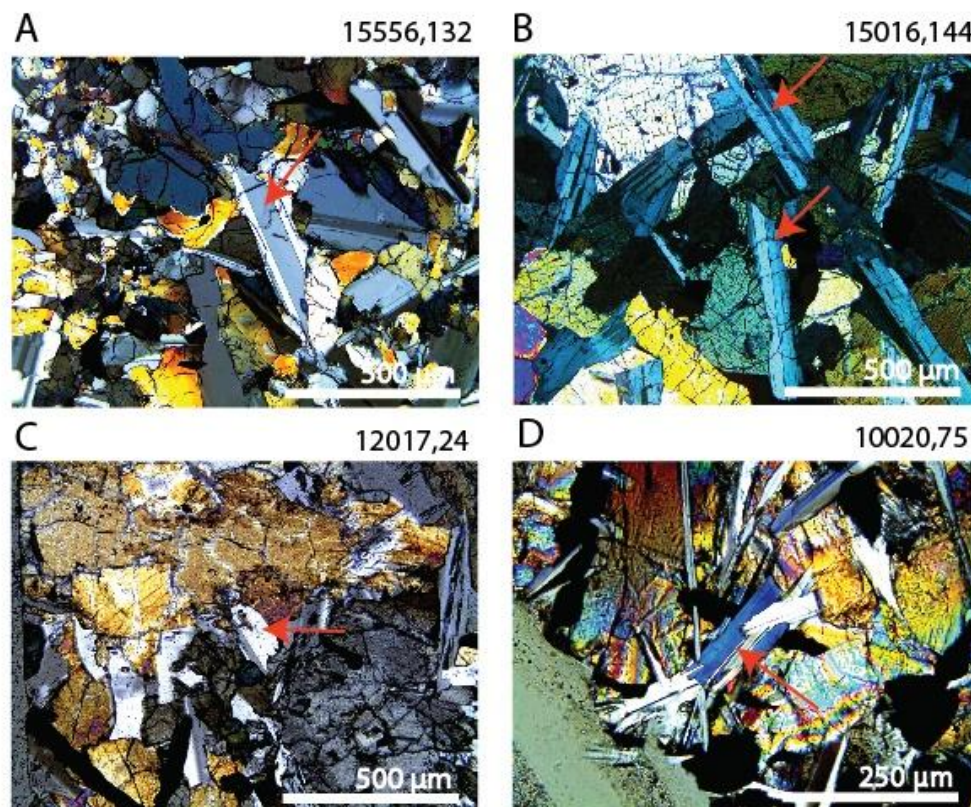


Figure S3. Representative petrographic textures of samples observed from transmitted light (cross polars) for 30 µm thin sections of four lunar basalts. (A) 15556,132. (B) 15016,144. (C) 12017,24. (D) 10020,75. Red arrows indicate representative plagioclase crystals used for cooling rate determinations in this study.

differentiate between impact generated fields and a long-lived dynamo field as the source of their NRM. By comparison, 10020 and 76535 provide high-fidelity records and their slow cooling rates imply a dynamo origin for the magnetizing fields.

2.2. Metal compositions. In order to assess the composition of magnetic carriers in our samples, we measured the relative Fe and Ni contents of metal in our samples using wavelength dispersive spectroscopy at the MIT Electron Microprobe Facility (Table S2). Metal was typically present either as isolated grains or in association with troilite.

Table S2. Elemental abundances of Fe and Ni in kamacite.

Thin Section	Fe (%)	Ni (%)	Notes
15556,130	99.30	0.70	assoc. w/troilite
15556,130	94.35	5.65	
15556,130	94.45	5.56	
15016,18	98.80	1.20	assoc. w/troilite
15016,18	92.35	7.66	
15016,18	86.47	13.53	
10020,75	100.00	0.00	assoc. w/troilite
10020,75	100.00	0.00	assoc. w/troilite
10020,75	100.00	0.00	
12017,63 basalt	100.00	0.00	assoc. w/troilite
12017,63 basalt	100.00	0.00	assoc. w/troilite
12017,63 basalt	99.23	0.77	
12017,63 basalt	99.25	0.75	
12017,63 glass	100.00	0.00	

Note: The first column lists the sample and thin section used for the analyses. The second and third columns contain the normalized (to Fe + Ni = 100%) elemental abundances of Fe and Ni in percent, respectively. The fourth column lists whether the metal grains observed were associated with troilite.

3. Domain State

3.1. Hysteresis data. We measured hysteresis loops for our samples using either a Digital Measurement Systems vibrating sample magnetometer (VSM) 1660 in C. Ross's lab in the MIT Dept. of Materials Science and Engineering or a Princeton Instruments MicroMag VSM in the paleomagnetism laboratory at CEREGE, Aix-en-Provence, France. Hysteresis parameters are shown in Table S3. The coercivity of remanence (H_{cr}) was determined either from remanence curve measurements at CEREGE or by analyzing coercivity spectra from rock magnetic experiments taken at MIT (see Section 4 of this document). A representative hysteresis loop depicting a multidomain magnetic mineralogy is shown for sample 15556 (Fig. S4).

Table S3. Magnetic hysteresis parameters for samples 15556, 15016, 12017, 10020, and 76535 from this and previous studies.

Sample	M_{rs}/M_s	$M_{rs} (Am^2/kg)$	$M_s (Am^2/kg)$	H_{cr}/H_c	$H_{cr} (mT)$	$H_c (mT)$	Source
15556							
221d	5.2×10^{-3}	6.1×10^{-4}	1.0×10^{-1}	24.0	32.2	1.3	this study
38-1	6.4×10^{-3}	7.0×10^{-4}	1.1×10^{-1}				Nagata et al. (1972, 1973)
38-2	1.7×10^{-4}	1.9×10^{-5}	1.1×10^{-1}		41.5	1.0	Nagata et al. (1972, 1973)
	3.7×10^{-3}	3.8×10^{-4}	1.0×10^{-1}	23.0	30.8	1.3	Gattacceca et al. (2010)
	4.5×10^{-3}	4.5×10^{-4}	1.0×10^{-1}	25.4	37.1	1.5	Gattacceca et al. (2010)
15016							
225S2	7.0×10^{-3}	4.8×10^{-4}	6.9×10^{-2}	16.1	38.4	2.4	this study
29-1	5.0×10^{-3}					2.7	Pearce et al. (1973)
a	3.4×10^{-3}	4.2×10^{-4}	1.3×10^{-1}	27.5	33.0	1.2	Cournede et al. (2012)
b	4.5×10^{-3}	3.9×10^{-4}	8.8×10^{-2}	19.2	25.0	1.3	Cournede et al. (2012)
12017 basalt							
12A2	5.0×10^{-3}	1.3×10^{-3}	2.6×10^{-1}	17.5	17.8	1.0	this study
glass							
12B	3.9×10^{-3}	2.7×10^{-3}	6.9×10^{-1}			2.5	this study
10020							
234c	1.2×10^{-2}	1.5×10^{-3}	1.3×10^{-1}	8.1	38.2	4.7	this study
76535							
137,1	1.6×10^{-2}			9.0			Garrick-Bethell et al. (2009)
137,3	2.7×10^{-2}			3.0			Garrick-Bethell et al. (2009)

Note: The first column identifies the subsamples studied from each parent rock. The second column displays the value of the saturation remanent magnetization (M_{rs}) divided by the saturation magnetization (M_s). The third column displays the value of the coercivity of remanence (H_{cr}) (see Section 4 and Table S4) divided by the coercive force (H_c). The fourth column shows the sources of reported values.

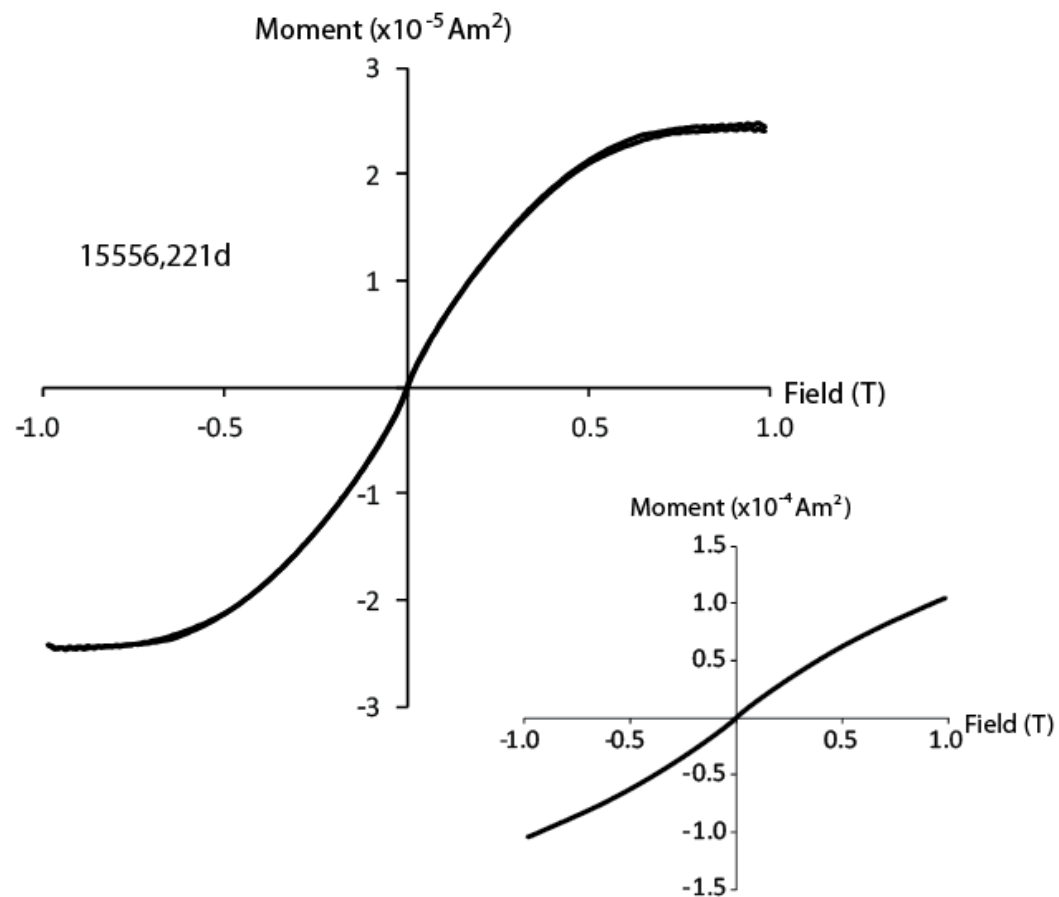


Figure S4. Representative magnetic hysteresis curve for sample 15556,221d. The top left figure shows the hysteresis curve for which a paramagnetic slope correction has been applied. The bottom right figure displays uncorrected data.

3.2. First order reversal curves. Following Pike et al. (1999), we also measured first order reversal curves (FORCs) for one subsample from each basalt in order to understand the distribution of domain states within our samples (Fig. S5). FORC measurements were made on a Princeton Instruments MicroMag VSM at the University of Minnesota Institute for Rock Magnetism. FORC distributions are plots of the range of magnetostatic interactions (H_u) vs. the distribution of coercivities (H_c). Our FORC distributions span the range $H_u = -10$ mT to 10 mT and $H_c = 0$ mT to 40 mT for all samples except for 15556,221d where we used the range $H_u = -20$ mT to 20 mT. FORC data were processed using the FORCinel software package (Harrison and Feinberg, 2008) using smoothing factors ranging from 6 to 10, depending on the sample when processing data with FORCinel.

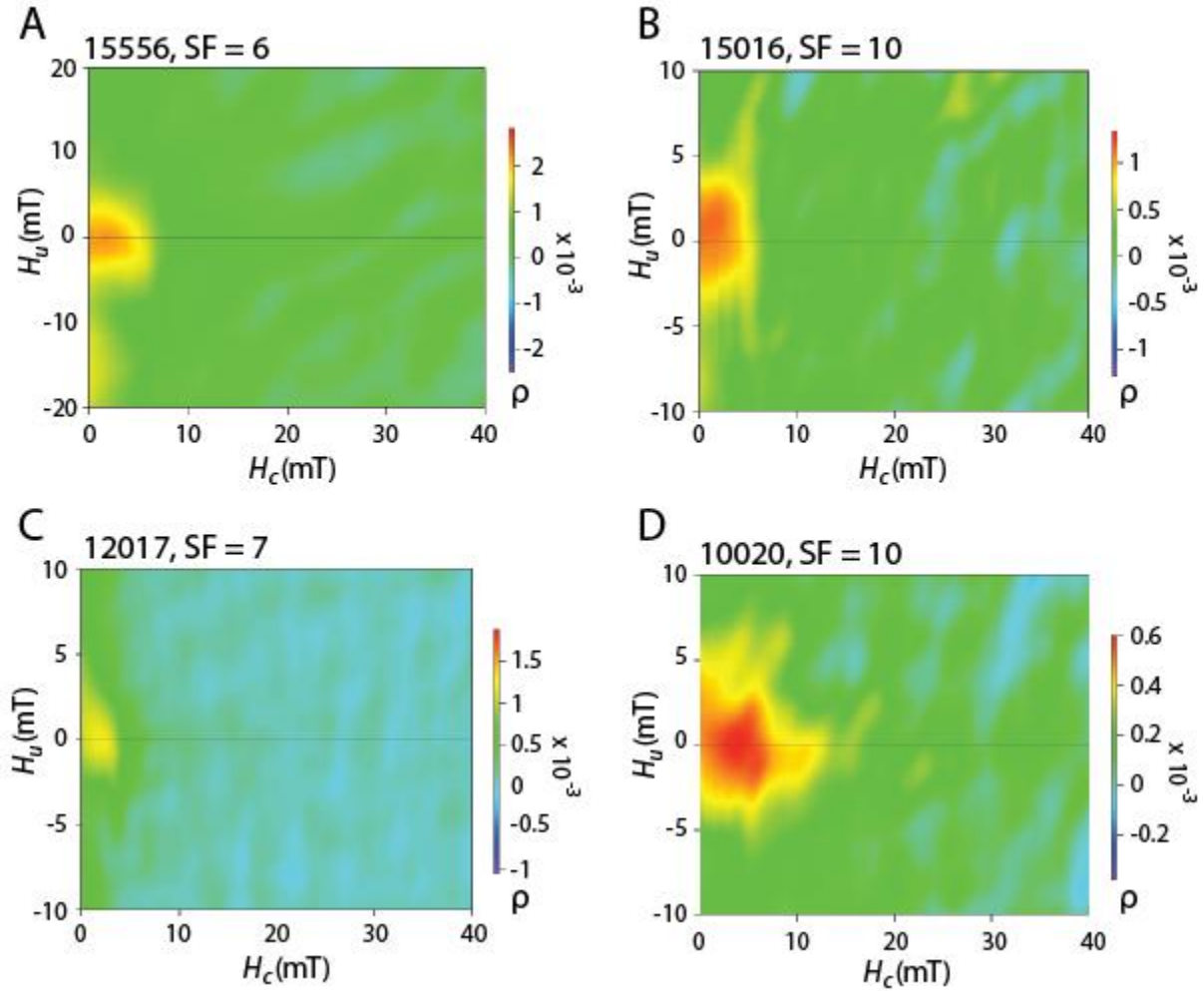


Figure S5. FORC diagrams of selected lunar samples. (A) 15556,221d. (B) 15016,225s2. (C) basalt 12017,12a2. (D) 10020,234c. FORC diagrams display H_u (degree of magnetostatic interactions) on the ordinate, H_c (coercivity) on the abscissa, and ρ (probability density of hysterons belonging to a given H_u and H_c) associated with the color bar. FORC diagrams were generated using the FORCinel software package (Harrison and Feinberg, 2008) using smoothing factors (SF) ranging from 6 to 10, depending on the sample.

4. Rock Magnetic Experiments

We performed additional rock magnetic characterization experiments on subsamples 15556,221a, 15016,b21, basalt 12017,13b1, glass 12017,13a2, and 10020,234b4. To determine the extent of magnetostatic interactions, each sample was progressively given ARM using an AC field of 200 mT and DC bias fields incrementally increasing from 0 to 2 mT (Cisowski, 1981). The final applied ARM (peak AC field = 200 mT, DC field = 2 mT) was then AF demagnetized at increasing fields to 290 mT. This provided us with the median destructive field (MDF) (Dunlop and Ozdemir, 1997) of ARM for each sample. Similarly, we applied a 200 mT isothermal remanent magnetization (IRM) field which was also stepwise AF demagnetized to 290 mT. From this we determined the MDF of IRM for each sample. This was followed by stepwise IRM acquisition to 886.5 mT and subsequent AF demagnetization to 290 mT. Acquisition and demagnetization of IRM provides information on coercivity spectra (Egli, 2003) (Fig. S6). These data also allowed us to determine the coercivity of remanence (H_{cr}), the field at which the normalized IRM acquisition and sIRM demagnetization curves intersect (Fig. S6a). Rock magnetic parameters derived from these experiments are shown in Table S4.

Table S4. Rock magnetic parameters.

Sample	sIRM/mass (Am^2/kg)	H_{cr} (mT)	Cisowski R value	MDF_{IRM} (mT)	MDF_{ARM} (mT)
15556,221a	5.15×10^{-4}	34.6	0.31	15.49	10.46
15016,225b21	5.50×10^{-4}	25.9	0.30	11.43	2.22
12017,13b1 basalt	1.71×10^{-4}	15.6	0.31	6.87	3.49
12017,13a2 glass	8.10×10^{-4}	143.4	0.38	2.54	28.21
10020,234b4	1.10×10^{-3}	46.5	0.31	21.72	20.62

Note: The first column gives the subsample name. The second column shows the saturation remanent magnetization normalized by mass. The third column shows the coercivity of remanence. The fourth column shows the Cisowski R value (Cisowski, 1981). The fifth and sixth columns show the M (AF required to reduce magnetization by a factor of 2) for sIRM and ARM (AC field 200 mT, DC field 2 mT), respectively (Dunlop and Ozdemir, 1997). Data for sample 10020,234b4 are taken from Shea et al. (2012).

5. AF demagnetization and Spurious Remanence

5.1. Introduction.

Prior to our paleomagnetic analyses on 15556, 15016, and 12017, we sanded the Johnson Space Center saw cut faces of the subsamples in order to remove surface contamination from the saw blade which could affect magnetic behavior. AF demagnetization experiments were conducted on mutually oriented subsamples from each parent rock. During these experiments, the magnetic moment of the samples was measured after AF application in each of the three orthogonal directions. The final moment for each AF level was calculated by taking the average of all measurements for the AF level, following the Zijdeveld-Dunlop method (Stephenson, 1993). This averaging was done in order to mitigate the effects of spurious ARM and GRM. All AF demagnetization-related data for 10020 presented here are sourced from Shea et al. (2012).

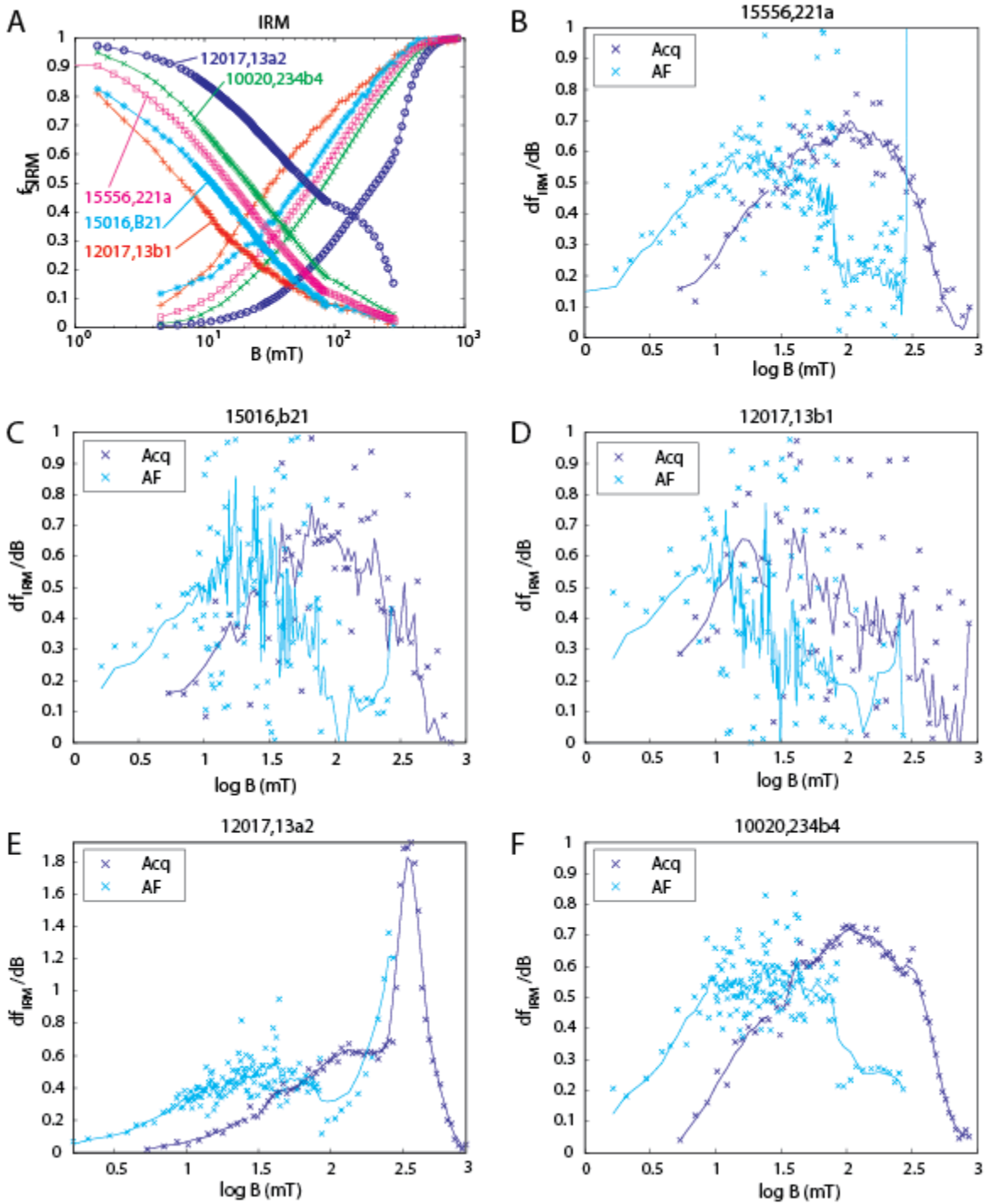


Figure S6. Stepwise acquisition and AF demagnetization of IRM. (A) Compilation of moment normalized IRM acquisition and AF demagnetization curves for all samples. Remaining figure parts display coercivity spectra of samples [i.e., derivative of IRM acquisition (dark blue curve) and AF demagnetization of IRM (light blue curve)]: (B) 15556,221a (C) 15016,b21, (D) basalt 12017,13b1, (E) glass 12017,13a2, and (F) 10020,234b4. Data for sample 10020,234b4 are taken from Shea et al. (2012).

5.2. *GRM*. In the main text, we describe how ARM may be a significant source of unstable demagnetization behavior in our lunar samples. Here, we will discuss the relevance of spurious GRM to our results. Spurious GRM can be acquired by anisotropic samples during static three-axis AF demagnetization. We tested for GRM in samples 15556, 15016, 12017, and 10020 by analyzing the difference in magnetization inclination between AF applications along the x , y , and z directions during demagnetization of NRM. This follows a similar analysis described by Garrick-Bethell et al. (2009) (see Section 3.2 of their Supplementary Online Material). We found that the inclination of magnetization after AF demagnetization in the z direction was not consistently shallower compared to that after demagnetization in the x and y directions (Fig. S7). This suggests that GRM does not significantly contribute to spurious demagnetization in our samples. While the test described here could fail to detect GRM if the x , y and z -axis AF orientations happen to coincide with the samples' principal axes of anisotropy, GRM is unlikely to be a major factor for any of these samples because they are all multidomain and GRM is more often associated with single-domain and pseudo-single-domain grains (although GRM in troctolite 76535 shows that this is not a requirement [see Garrick-Bethell et al., 2009]).

5.3. *NRM demagnetization data*. Using the Zijderveld-Dunlop averaged AF demagnetization data, we identified low coercivity (LC) and high coercivity (HC) magnetic components in subsamples. Magnetization directions and maximum angular deviations (MADs) were computed for the LC and HC components using principal component analysis (PCA) (Kirschvink, 1980) (Table S5). Several subsamples lacked easily identifiable magnetic components; in such cases, we defined somewhat arbitrary components to be used during paleointensity computations (see Section 6). The demagnetization results for each sample are discussed individually below:

5.3.1. *Mare basalt 15556*

We found that three of our five subsamples of 15556 have two poorly defined NRM components: an LC component blocked from NRM to 3-5 mT, and an HC component ranging from the upper end of the LC component up to 6-19 mT (depending on the subsample) (Table S5 and Fig. 3a). Of the remaining two, subsample 15556,220a lacked an obvious HC component; we therefore tentatively computed a HC component fit spanning 4-50 mT for the purposes of computing paleointensities (Section 4.2). The LC components of 15556,221a and 15556,221d were approximately unidirectional (overlapping MAD circles) with respect to each other, but not with respect to the LC components of the other subsamples from 15556 (Fig. S8a). The dANG/MAD test suggested that the only subsample with an origin-trending HC component was 15556,221a (Table S6). The HC directions for the three subsamples in which they were reasonably well-defined were scattered (their MAD circles did not overlap) (Fig. S8a). For coercivities above 6-19 mT, the remaining NRM is overwhelmed by spurious ARM. This behavior is consistent with previous AF demagnetization studies on 15556 (Gattacceca et al., 2010; Nagata et al., 1973), which observed a LC magnetic component blocked between 0-5 mT and a possible HC component blocked between 5 mT and 20 mT. These HC components also exhibited unstable remanence.

The other sample without two NRM components was our smallest subsample, 15556,221c. This sample displayed a spectacular example of magnetic pinning (Figs. 3b and

S9). Its NRM remained stable up to 3 mT, but at higher fields (from 3.5 to 240 mT) switched back and forth between two nearly perfectly antipodal directions 439 times out of 975 demagnetization steps applied at 116 different AF field levels between 1.5 mT and 290 mT.

5.3.2. Mare basalt 15016

The AF demagnetization behavior of 15016 was inconsistent among our six subsamples (Table S5, Fig. 3c). All subsamples exhibited spurious demagnetization behavior similar to that described for 15556. Two subsamples had no clearly identifiable magnetic components. Three subsamples had LC components blocked between NRM and a maximum of 4.5 mT, but no obvious HC component. The LC components were non-unidirectional across subsamples (Fig. S8b). Only 15016,225s2, had two identifiable components: an LC component blocked between NRM and 9 mT, and an HC component blocked between 9 mT and 17.5 mT which fails the dANG/MAD test (Table S6). The assigned LC and HC components spanned between NRM and a maximum of 9.5 mT, and from the end of the LC component to 43 mT, respectively. Previous AF demagnetization studies conducted on by Pearce et al. (1973) and Cournede et al. (2012) showed unstable demagnetization characteristics similar to those observed here.

5.3.3. Mare basalt 12017

Subsamples from the basalt portion of 12017 had clearly identifiable LC components, typically blocked between NRM and 8.5 mT [see Buz et al., (2011); detailed NRM demagnetization data to be presented elsewhere]. Because spurious demagnetization obscured any HC components in the basalt samples, for the purposes of our paleointensity tests (Section 4.2) we computed nominal HC components ranging from the end of the LC components to a maximum of 80 mT (Table S5 and Fig. 3d). The computed HC magnetization directions for 12017,12a2 and 12017,12a1c were roughly unidirectional (MADs overlapped), but neither passed the dANG/MAD test (Table S6). Previous AF demagnetization experiments by Strangway et al. (1971) on two 12017 subsamples identified two NRM components blocked up to 5 mT and from 5 mT to 20 mT, respectively. The moment magnitude increased and decreased erratically with increasing peak AF fields above 5 mT. At 20 mT, the magnetization direction of subsamples 12017,4 and 12017,5 were roughly unidirectional (within ~30° of one another), consistent with our own observations of 12017. Our AF demagnetization of the 12017 glass yielded LC components between NRM and 8.5 mT. Stable HC magnetizations could not be identified, so we assigned tentative components blocked to AC fields of ~85 mT (Table S5, Fig. 3e). With exception of basalt subsample 12017,12a1c, the LC component directions for all subsamples of 12017 (basalt and glass) were roughly unidirectional.

5.3.4. Mare basalt 10020

10020 has two magnetization components [detailed demagnetization presented in Shea et al. (2012)]. LC components were blocked from NRM to 8.5-17 mT, depending on the subsample, while HC components were blocked up to between 75 mT and > 290 mT. The LC components were not unidirectional across the entire sample. The high coercivity magnetization of 10020 is consistent with prior AF demagnetization study (Collinson et al., 1972; Fuller and

Cisowski, 1987). As described in detail in Shea et al. (2012), 10020 has an extraordinarily stable magnetization [even exceeding that observed for 76535 (Garrick-Bethell et al., 2009)].

Table S5. PCA for AF demagnetization on subsamples of 15556, 15016 and 12017.

Sample	Mass (mg)	Type	Range (mT)	N	Dec. (°)	Inc. (°)	MAD (°)	Forced?
15556								
220a	31.5	LC	NRM-4.0	8	279.1	-10.9	14.7	No
		HC*	4.0-50.0	57	150.3	-52.4	32.7	Yes
221a	461.9	LC	NRM-6.5	21	33.0	20.9	18.6	No
		HC	6.5-19.0	26	256.9	-77.4	12.3	Yes
221c	17.0	1st pin			334.9	38.6	27.7	
		2nd pin			149.2	-51.5	31.6	
221d	203.7	LC	NRM-5.5	14	42.2	13.4	23.0	No
		HC	5.5-10.5	11	290.3	-29.0	23.4	Yes
221g	112.7	LC	NRM-8.5	21	68.3	-1.5	10.4	No
		HC	8.5-22.5	29	288.2	5.4	14.2	Yes
15016								
225s1	100.5	LC*	NRM-9.5	18	180.3	29.7	28.4	No
		HC*	10.0-43.0	49	274.6	-9.9	25.6	Yes
225s2	359.4	LC	NRM-9.0	17	271.6	-29.0	22.3	No
		HC	9.0-17.5	18	229.0	10.0	15.4	Yes
225b21	104.3	LC*	NRM-5.5	10	159.1	-35.8	12.4	No
		HC*	6.0-43.0	57	324.8	25.2	29.1	Yes
225b22	165.8	LC	NRM-4.5	8	109.5	-45.7	20	No
		HC*	4.5-6.5	5	290.1	47.6	14	Yes
225b23	207.8	LC	NRM-3.5	6	212.8	2.5	32.7	No
		HC*	4.0-43.0	61	252.8	30.7	33.8	Yes
225b24	157.8	LC	NRM-3.5	10	197.7	-42.1	20.4	No
		HC*	3.5-14.5	23	280.0	-12.0	29.6	Yes
12017 basalt								
12a2	183	LC	NRM-8.5	16	294.5	33.7	12.0	No
		HC*	8.5-69.0	77	145.7	48.1	29.1	Yes
12a1c	104.3	LC	NRM-8.0	15	239.9	81.0	11.0	No
		HC*	8.5-64.0	73	127.0	42.6	39.5	Yes
13b1	131.6	LC	NRM-11.5	21	263.8	-17.4	36.9	No
		MC*	12.0-54.0	66	121.0	-70.7	35.4	No
		HC*	54.0-80.0	26	144.9	26.9	22.0	Yes
glass								
12b	27.1	LC	NRM-8.5	16	277.8	24.7	9.8	No
		HC*	9.0-85.0	75	346.8	-65.1	20.5	Yes
13a2	49.5	LC	NRM-8.5	16	269.9	21.1	14.0	No
				10				
		HC*	8.5-85.0	3	206.4	-78.6	23.0	Yes
	15							
59	(est.)	LC1	NRM-4.5	7	180.0	-11.4	9.4	No

MC	5.0-9.0	9	303.6	-3.9	15.8	No
HC*	9.5-39.0	56	146.5	74.6	13.3	Yes

Note: The first column contains sample and subsample names. The second column shows the mass of each subsample. The third column designates whether the row describes the low coercivity (LC), medium (MC), or high coercivity (HC) components of magnetization in the sample. Asterisks (*) indicate that the specified magnetic component was not clearly identified for that sample and that an AF range has been tentatively assigned to represent a hypothetical HC component for the purpose of paleointensity estimations. The fourth column contains the AC field values bounding the components identified for each subsample (except for 15556,221c, where it indicates the location of magnetic pinning in that subsample). The fifth column shows the number of points (i.e., AF steps) used in the PCA calculation for each component. The sixth, seventh, and eighth columns show the mean declination, mean inclination, and the MAD, respectively, for each component. The ninth column indicates whether the component was forced through the origin during the PCA calculation.

The dANG/MAD test allows one to qualitatively determine whether a component of magnetization is origin-trending (Lawrence et al., 2008). As mentioned in the main text, the dANG/MAD test works by comparing the value of the angular difference between an unconstrained PCA fit of the NRM component and the centroid of the least squares fit (dANG) to the MAD of the PCA fit. If $dANG < MAD$ for a given magnetic component, then the component is trending toward the origin (pass). If $dANG > MAD$, the component is not origin-trending (fail). Using the dANG/MAD test on samples with noisy demagnetization data is tenuous because demagnetization of such samples will usually result in the calculation of large MADs. This may cause samples to yield false positives when using the dANG/MAD test. Alternatively, the effects of spurious AF demagnetization may obscure what would otherwise be an origin-trending magnetic component, invariably yielding a negative result.

We conducted dANG/MAD testing on HC components (easily identified HC components, as well as tentative HC components assigned to subsamples with poor demagnetization behavior) for samples 15556, 15016, and 12017 (see Table S5 for components and corresponding AF AC field ranges). We computed dANGs and MADs for two cases. In the first case, dANG and MAD were computed for the full range of AF steps of HC components. In the second case, dANG and MAD were computed for a limited range of AF steps. This was done to see if spurious ARM (which would be preferentially acquired at higher AF steps) would cause samples to pass the dANG/MAD test when they would otherwise fail if the AF range were restricted. For samples with more than 10 AF steps in their HC components, dANG and MAD were calculated using the first 10 AF steps in the component. For samples with fewer than 10 AF steps in their HC components, only the first 5 steps were used to calculate dANG and MAD (Table S6).

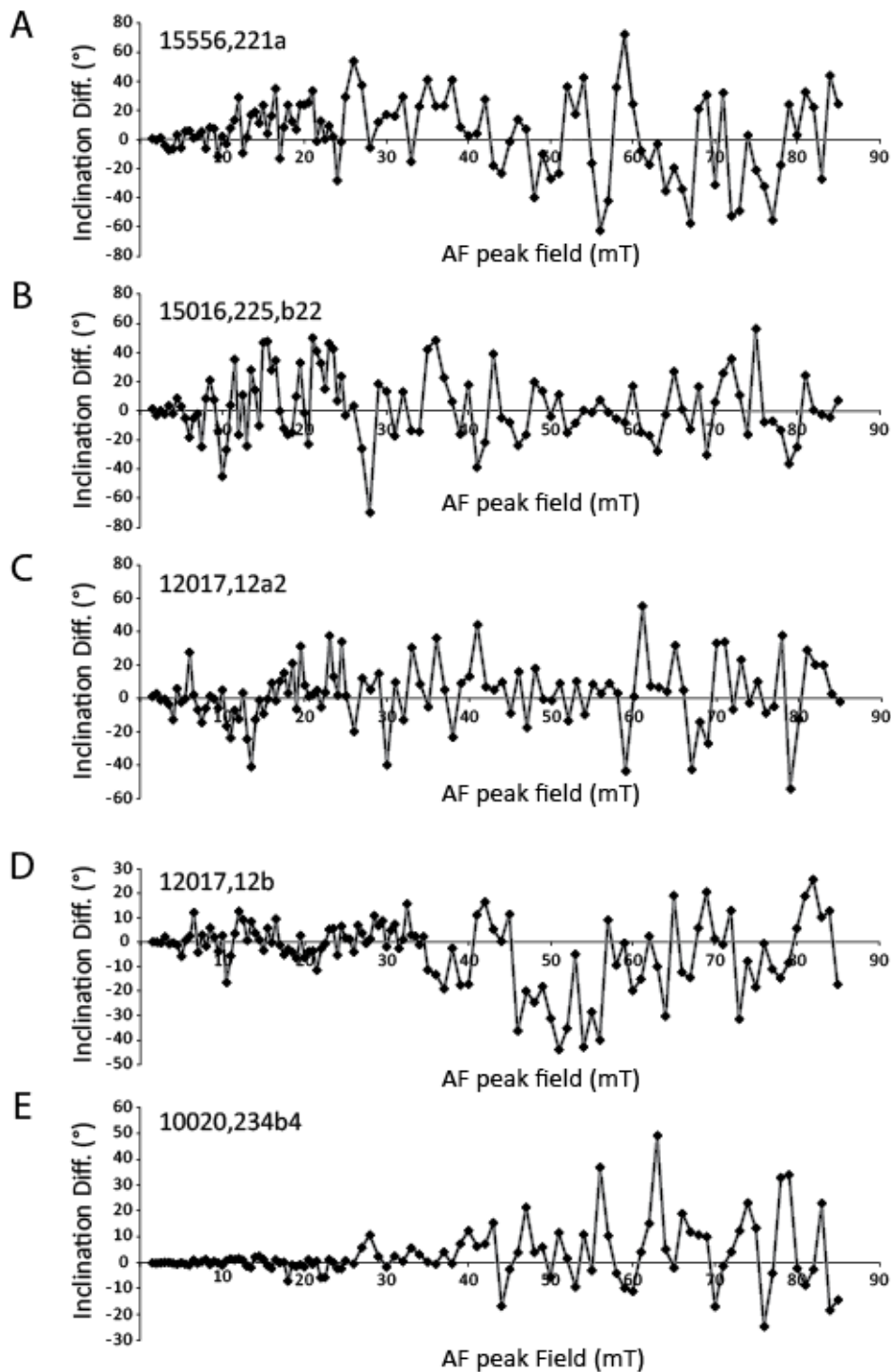


Figure S7. GRM analysis of samples (A) 15556,221a, (B) 15016,225,b22, (C) basalt 12017,12a2, (D) glass 12017,12b, and (E) 10020,234b4. The ordinate of the figure shows the difference in magnetic inclination between uniaxial AF demagnetization along the z -axis and preceding AF demagnetizations along the x - and y - orthogonal axes at a given AF step (figure abscissa). If spurious GRM was present, there would be a monotonic rise in inclination difference with increasing AF fields. Since this pattern does not appear in our demagnetization data, GRM is not a substantial contributor to unstable AF demagnetization in these samples. The increasing variability in inclination difference with AF level is a manifestation of growing spurious ARM noise.

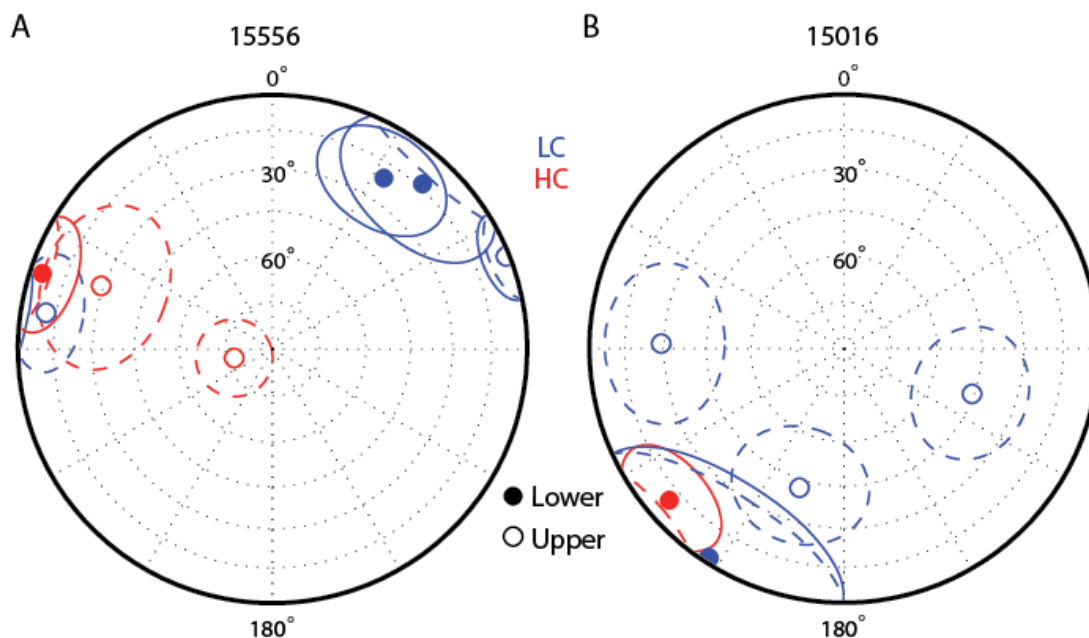


Figure S8. Equal area stereographic projection of NRM components fit to samples (A) 15556 and (B) 15016. Blue and red circular points denote LC and HC directions for subsamples, respectively. Open circles represent points in the upper hemisphere, while filled in circles designate points in the lower hemisphere. Surrounding ellipses denote the MAD for each component direction.

Table S6. Origin-trending test for HC components of lunar samples.

Sample	<i>Full Component</i>			<i>Truncated Component</i>		
	dANG	MAD	Pass?	dANG	MAD	Pass?
15556						
220a*	62.2	35.9	No	68.2	11.5	No
221a	21.7	30.5	Yes	25.2	23.6	No
221d	57.4	39	No	42	27.9	No
221g	27.2	20.2	No	33.6	19.3	No
15016						
225s1*	58.2	37.1	No	63	32.1	No
225s2	30.7	21.9	No	31.7	23.6	No
225b21*	30.7	33.1	Yes	26.9	33.4	Yes
225b22*	20.2	20.2	Yes(?)			
225b23*	36.8	43.2	Yes	74.4	43.6	No
225b24*	54.9	51.3	No	81.8	44.6	No
12017 basalt						
12a2*	74.1	38.4	No	73.3	37.1	No
12a1c*	47.5	35.2	No	44.2	22.3	No
glass						
12b*	18.2	40.7	Yes	44.7	40.9	No
13a2*	52.5	30	No	32.7	28.3	No
59*	65.5	45.5	No	51	33.2	No

Note: The first column contains sample and subsample names. The second, third, and fourth columns contain the dANG, MAD, and whether dANG < MAD (pass) for the full range of HC component AF fields, respectively. The fifth, sixth, and seventh columns contain the dANG, MAD, and whether dANG < MAD for the first 10 (or 5, see preceding text) AF steps of the HC component, respectively. Asterisks (*) indicate samples without a clearly identifiable HC component and that were assigned tentative HC components (see Table S3).

Only one basalt sample with a clearly identifiable HC component (15556,221a) passed the dANG/MAD test for origin-trending magnetization. Alternatively, samples with no obvious HC component (15016,225b21, 15016,225b22, and 15016,225b23) ended up passing the dANG/MAD test. This is likely due to the large MADs associated with the corresponding PCA fits of assigned components. Most samples which passed the dANG/MAD test when PCA was conducted on the full range of AF steps belonging to the component failed when PCA fits were only conducted on the first few AF steps. We believe this may have occurred for two reasons: (1) the reduced number of points incorporated into the PCA fit made it more difficult for PCA to register directional trends in the data, and (2) using a smaller number of data points may have resulted in a lower MAD when compared to the dANG value.

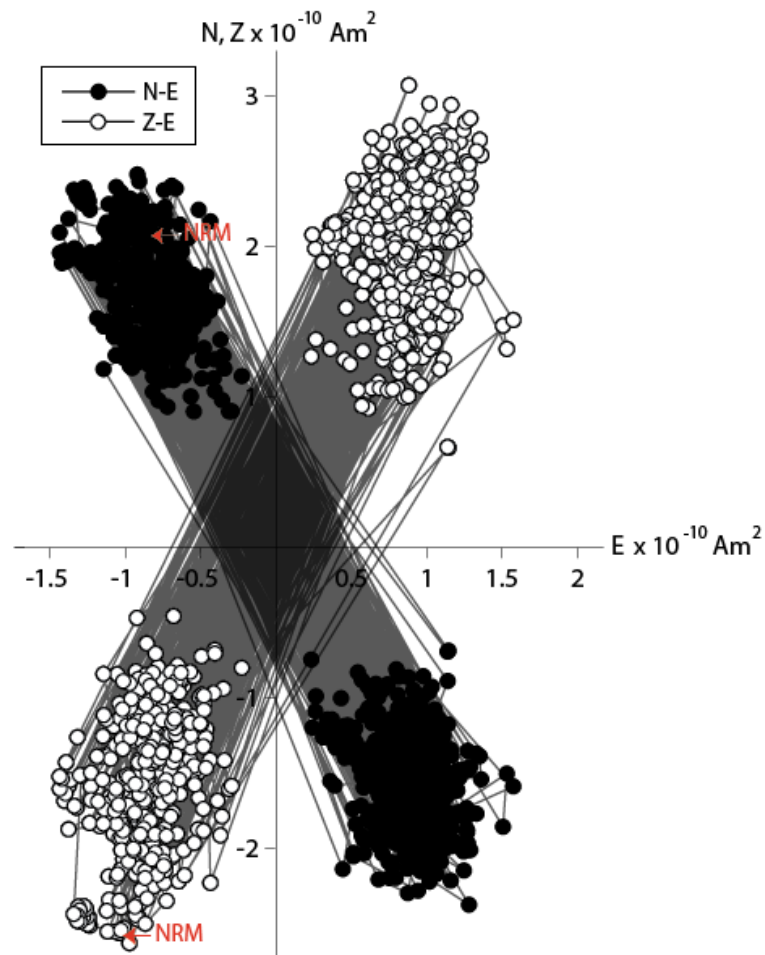


Figure S9. Complete, unaveraged, NRM demagnetization of sample 15556,221c up to 290 mT. Shown is a two-dimensional projection of the NRM vector during AF demagnetization. Closed symbols represent end points of magnetization projected onto the horizontal (N and E) plane. Open symbols represent end points of magnetization projected onto the vertical (N and Z) plane. Red arrows indicate the position of the NRM vector.

6. Paleointensity Experiments and Limit Tests

6.1. ARM and IRM paleointensity techniques. In the ARM method, progressive AF demagnetization of NRM is compared to partial ARM acquisition (Stephenson and Collinson, 1974; Stephenson et al., 1977). This relationship is expressed as:

$$\text{ARM paleointensity in } \mu\text{T} = \frac{\Delta\text{NRM}}{\Delta\text{ARM}} \cdot \frac{(\text{bias field in } \mu\text{T})}{f_{\text{ARM}}} \quad (1)$$

for an experimentally determined value of the TRM to ARM ratio, f_{ARM} . Apollo-era implementations of this method did not utilize vector component subtraction of the NRM and so were strictly applicable to single component NRMs (Stephenson and Collinson, 1974). Here we use vector subtraction of the NRM to obtain multicomponent paleointensity values [see also Garrick-Bethell et al. (2009) and Weiss et al. (2008)]. To provide a redundancy check on our retrieved paleointensities, we applied ARM at three different DC bias fields: 0.05, 0.2, and 0.6 mT.

The above equation is analogous to that for the Thellier-Thellier paleointensity experiment but using ARM as an proxy for TRM (Thellier and Thellier, 1959). The value of f_{ARM} has been found for lunar rocks to typically fall between 0.9-1.6. However, f_{ARM} might be an order of magnitude higher than this for samples with elongate grains [see Garrick-Bethell et al. (2009) for review], and can range up to 19 for narrow size dispersions of pure magnetite crystals. We use $f_{\text{ARM}} = 1.34$ as determined for some lunar rocks by Stephenson and Collinson (1974). Because of uncertainty in the value of f_{ARM} , paleointensities calculated by the ARM technique may be off by a multiplicative factor of 2 to 5 for typical rocks with broad crystal shape and size distributions (Bailey and Dunlop, 1977; Dunlop et al., 1975; Yu, 2010). These uncertainties are nevertheless sufficient for determining meaningful paleointensities for a variety of extraterrestrial samples (Garrick-Bethell et al., 2009; Weiss et al., 2008).

A second method for determining paleointensities compares AF demagnetization of IRM induced in a strong field (either 200 mT or 886.5 mT, depending on the subsample) to the demagnetization of NRM, following Garrick-Bethell et al. (2009). Paleointensities are estimated from the relationship:

$$\text{IRM paleointensity in } \mu\text{T} = \frac{\Delta\text{NRM}}{\Delta\text{IRM}} \cdot f_{\text{IRM}} \quad (2)$$

where f_{IRM} is a calibration constant derived from the REM paleointensity method and has units of field. The value of f_{IRM} can vary by up to a factor of ~ 50 , depending on size, shape, and microcoercivity distributions. Stephenson et al. (1977) determined f_{IRM} to be $\sim 3800 \mu\text{T}$ for several lunar samples, while Cisowski et al. (1983) measured f_{IRM} to be $\sim 4700 \mu\text{T}$. More recently, estimates of $f_{\text{IRM}} \sim 3000 \mu\text{T}$ and $f_{\text{IRM}} \sim 2780 \mu\text{T}$ have been published by Gattacceca and Rochette (2004) and Yu (2010), respectively, for a variety of terrestrial and extraterrestrial lithologies. In this paper, we use $f_{\text{IRM}} = 3000 \mu\text{T}$ for our IRM paleointensity determinations. It has been shown that the IRM method is capable of accurately retrieving paleointensities (when magnetite is the magnetic carrier) from TRM acquired at fields as low as $0.15 \mu\text{T}$ (Yu et al., 2007), although this finding is at odds with the results of Kletetschka et al. (2006), which suggested that many multidomain samples cannot properly record TRM at fields below 1-10 μT . The IRM method may be slightly more reliable than ARM paleointensities because the IRM

method is less volume concentration and grain-size dependent, and is more stable against AF demagnetization (Yu, 2010).

We quantified formal paleointensity uncertainties by computing 95% confidence intervals using a two-tailed Student's *t*-test (Weisberg, 1985) on the linear slopes of NRM lost vs. ARM gained or sIRM lost. This formal uncertainty only represents that associated with the linear regression and does not take into account systematic uncertainties associated with the unknown values of f_{IRM} or f_{ARM} . Its main use is to demonstrate whether the paleointensity values are distinguishable from zero (e.g., demonstration that ancient field was not null). As discussed above, the systematic uncertainties associated with f_{ARM} and f_{IRM} actually dominate the total uncertainty.

6.2. NRM paleointensity determinations. Using the ARM and IRM methods described in the preceding section, we computed absolute paleointensities for the LC and HC magnetization components of subsamples from 15556, 15016, and 12017. Since we cannot be sure that the HC magnetizations in any of these samples are actually TRMs, we only report values for the slopes $\Delta\text{NRM}/\Delta\text{ARM}$ and $\Delta\text{NRM}/\Delta\text{IRM}$ (Table S7). In addition, we also computed paleointensities for one subsample from each rock for the AF range 23-85 mT which is greater than all easily identified HC component ranges for all samples. This was done in order to compute paleointensities from a coercivity fraction unlikely to have been overprinted by secondary remanence to be used in the construction of Fig. 6. Note that this range also coincides with AF fields where these subsamples expressed unstable behavior during demagnetization.

Table S7. $\Delta\text{NRM}/\Delta\text{ARM}$ and $\Delta\text{NRM}/\Delta\text{IRM}$ values for our lunar rocks using the ARM and IRM paleointensity methods.

		$\Delta NRM/\Delta ARM$			$\Delta NRM/\Delta IRM$
Sample	Component	0.05 mT	0.2 mT	0.6 mT	
15556					
220a	LC	3.78 ± 6.18	1.30 ± 0.82	0.61 ± 0.40	0.0747 ± 0.0334
	HC	-0.02 ± 0.26	0.04 ± 0.12	0.03 ± 0.06	0.0008 ± 0.0028
221a	LC	1.27 ± 0.64	0.33 ± 0.07	0.14 ± 0.04	0.0151 ± 0.0038
	HC	0.51 ± 0.14	0.28 ± 0.05	0.14 ± 0.02	0.0114 ± 0.0018
221d	LC	0.73 ± 1.05	0.66 ± 0.26	-	-
	HC	0.43 ± 0.63	0.29 ± 0.27	-	-
221g	LC	1.39 ± 0.60	0.26 ± 0.19	-	0.0130 ± 0.0076
	HC	0.70 ± 0.92	0.99 ± 0.15	-	0.0343 ± 0.0050
	23-85 mT	-0.06 ± 0.07	0.00 ± 0.10	-	0.0007 ± 0.0020
15016					
225S2	LC	0.64 ± 0.37	0.22 ± 0.06	-	0.0071 ± 0.0020
	HC	0.26 ± 0.41	0.34 ± 0.11	-	0.0105 ± 0.0026
225b21	LC	-0.09 ± 1.91	-0.03 ± 1.32	-	0.0057 ± 0.0677
	HC	0.12 ± 0.20	-0.19 ± 0.19	-	-0.0047 ± 0.0052
	23-85 mT	-0.06 ± 0.13	-0.09 ± 0.17	-	-0.0042 ± 0.0068
12017					
basalt					
12A2	LC	2.71 ± 1.55	1.03 ± 0.19	0.45 ± 0.08	0.0578 ± 0.0062
	HC	0.11 ± 0.13	0.11 ± 0.06	0.05 ± 0.03	0.0044 ± 0.0036
	23-85 mT	0.02 ± 0.23	0.25 ± 0.15	0.22 ± 0.11	0.0189 ± 0.0103

12A1C	LC	1.53 ± 0.64	0.90 ± 0.13	0.50 ± 0.08	-
	HC	0.14 ± 0.17	0.08 ± 0.09	0.03 ± 0.06	-
	23-85 mT	0.01 ± 0.17	0.03 ± 0.10	-0.01 ± 0.07	-
glass					
12B	LC	3.93 ± 1.24	1.11 ± 0.11	0.33 ± 0.04	-
	HC	0.17 ± 0.07	0.05 ± 0.02	0.02 ± 0.01	-
13A2	LC	0.85 ± 0.86	0.39 ± 0.19	0.14 ± 0.06	0.0986 ± 0.0111
	HC	0.24 ± 0.04	0.10 ± 0.01	0.04 ± 0.01	0.0043 ± 0.0013

Note: The first column lists the sample and subsample numbers. The second column designates whether the paleointensity experiment was conducted for the low coercivity (LC) component, high coercivity (HC) component, or a magnetization component defined by AF steps of 23-85 mT in the sample. The coercivity ranges for LC and HC components used in the paleointensity calculations are the same as those describing components in Table 1. The third, fourth, and fifth columns show $\Delta\text{NRM}/\Delta\text{ARM}$ values computed from paleointensity slope fits to the associated AF range using ARM acquisition with 0.05 mT, 0.2 mT, and 0.6 mT DC bias fields, respectively. The sixth column shows $\Delta\text{NRM}/\Delta\text{IRM}$ values computed from paleointensity slope fits to the associated AF range. All data reported are in the format slope \pm 95% formal confidence radius from Student's *t*-test.

6.3. Magnetic fidelity experiments. As described in detail in the main text, we conducted a series of simulated paleointensity experiments to assess the magnetic fidelity of our lunar samples. This procedure involved giving the samples a laboratory ARM (as an analog of TRM), AF demagnetizing this laboratory remanence, and then using the ARM paleointensity method to retrieve a value (i.e., paleointensity) for the strength of the applied ARM field. A sample was defined to have high magnetic fidelity at fields where the percentage difference between the retrieved paleointensity and the laboratory field (*D*) as well as the percentage difference between the formal 95% confidence interval and the laboratory field (*E*) were both less than 100%. In general, we observed that samples preserved higher fidelity magnetizations at stronger ARM DC bias fields. As an example of this, we show a comparison between AF demagnetization of ARM acquired at DC bias fields of 3 μT and 200 μT (Fig. S10). The demagnetization of the 200 μT remanence is clearly more stable than that of the 3 μT , which exhibits noisy demagnetization behavior.

A possible complication with the paleointensity fidelity experiments described in the main text is that the formal uncertainty of the inferred paleointensity may be artificially inflated due to spurious ARM imparted during application of the ARM itself (e.g., the remanence that is subjected the paleointensity experiment). If so, then the minimum paleofield limits inferred above may in fact be overestimates, such that the rocks would be better recorders of TRM than our estimates suggest. To investigate this possibility, we ran the following series of experiments on one subsample of 15556,221g. We imparted ARM with varying AC field strengths (10 mT, 20 mT, 40 mT, and 85 mT), using a constant value of 50 μT for the DC bias field. After each ARM application, we demagnetized the sample to 10 mT and computed paleointensities using the ARM method. Our results show that the uncertainty (95% confidence interval) of the retrieved paleointensity value increased slightly with higher peak AC field during ARM application (Fig. S11), suggesting the influence of ARM noise. Since this increase in uncertainty was modest (from 8 μT to 12 μT), our estimates of the minimum recording capacities in the simulated paleointensity experiments discussed above are likely fairly accurate.

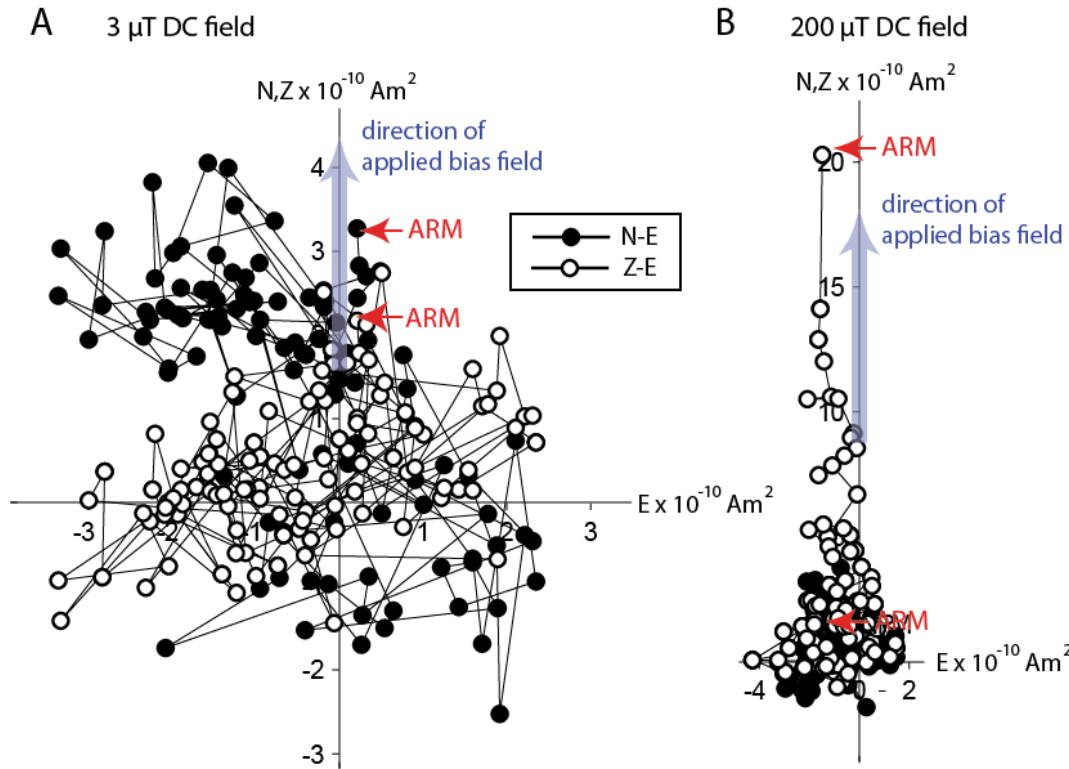


Figure S10. AF demagnetization of laboratory ARM produced in DC fields of (A) 3 μT and (B) 200 μT . Shown is a two-dimensional projection of moment vector during AF demagnetization. Closed symbols represent end points of magnetization projected onto the horizontal (N and E) plane. Open symbols represent end points of magnetization projected onto the vertical (N and Z) plane. Red arrows designate the point of ARM acquisition prior to commencing the demagnetization experiment. The applied bias field directions are shown with blue arrows.

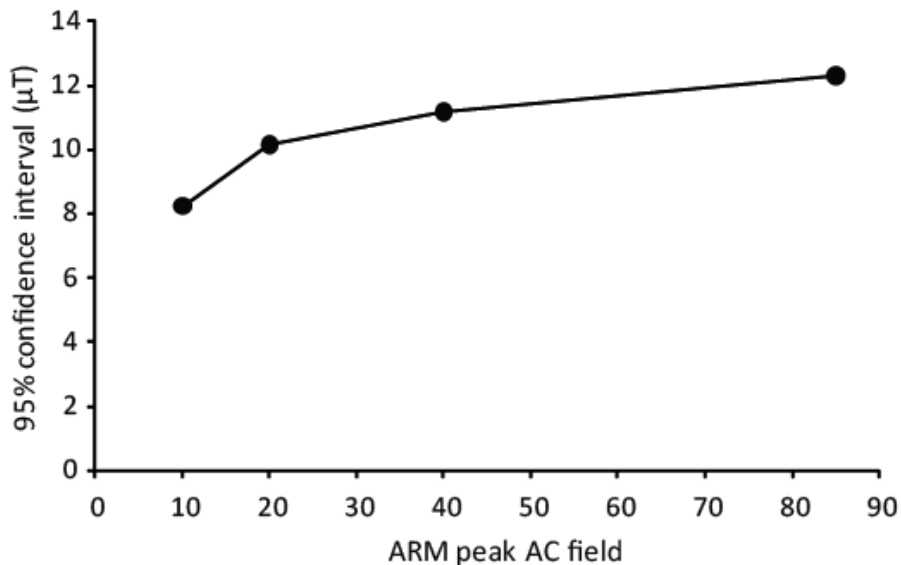


Figure S11. Width of formal 95% confidence intervals of retrieved paleointensities for applied laboratory ARM (0.05 mT DC field) at various peak AC fields (10 mT, 20 mT, 40 mT, and 85 mT). The widths of the 95% confidence intervals increased with peak AC field, suggesting an increased influence of ARM noise at higher peak AC fields.

6.4. REMc normalization method experiments. ARM was applied to samples using AC fields of 80 or 85 mT and DC fields ranging from 0.003 mT to 0.2 mT. Using $f_{\text{ARM}} = 1.34$ (see Section 6.1 above), this correlates to TRM acquisition at laboratory fields of 2-150 μT . We did not observe a linear trend for retrieved paleointensity vs. applied field when using the REMc normalization method (here computing $\text{ARM}_{20}/\text{sIRM}_{20}$ with ARM standing in as TRM) (Fig. 5). We ascribe this behavior to the acquisition of spurious ARM from the AF demagnetization steps associated with this technique.

We observed strong linear trends (correlation coefficients > 0.98) when computing ratios of undemagnetized ARM and sIRM for most samples (Fig. 5). However, the relationship between retrieved paleointensity and applied laboratory field was not 1:1 as expected for all samples. This likely occurred because of uncertainties associated with the unknown values of f_{ARM} and f_{IRM} for these samples. Variations in f_{ARM} and f_{IRM} may exist for different samples, and utilizing higher or lower values for these constants could result in a change in the slope of the retrieved paleointensity versus applied laboratory field line. Furthermore, since the ARM was only applied at AC fields of 80-85 mT as compared to the sIRM being applied at 886.5 mT, a comparison of total ARM to total IRM will lead to underestimated slopes in Figs. 5a and 5b because not all the high coercivity grains were magnetized by the ARM. For example, the slope of retrieved paleointensity versus applied paleofield for subsample 12017,13a2 is ~ 0.2 (Fig. 5b), which is $\sim 80\%$ less than the expected slope of 1. This underestimated slope is consistent with our IRM acquisition experiments, which suggest that $\sim 75\%$ of magnetization carrying capacity this subsample is carried between coercivities of 85 mT and 886.5 mT. Similarly, the slope for 10020,234d is underestimated by $\sim 33\%$ because $\sim 25\%$ of the magnetization carrying capacity of sample 10020,234d is carried by grains with coercivities between 200 mT and 886.6 mT. Lower coercivity samples should have slopes closer to 1 because a larger fraction of their magnetic carriers was initially magnetized by the ARM acquisition. Results from sample 15016 were an exception to this pattern of linearity (correlation coefficients < 0.98). 15016 is especially susceptible to spurious ARM (as evidenced by its high $\sim 37 \mu\text{T}$ paleofield recording limit; Fig. 4) and multidomain character (see Sections 3 and 4). We posit that spurious ARM acquired during the acquisition of laboratory ARM (the TRM analog) may be responsible for the nonlinearity associated with this sample's behavior during this experiment.

7. Anisotropy of remanence

7.1. Results from all samples. In order to assess the level of contribution of magnetic anisotropy to observations of noisy AF demagnetization in samples, remanence anisotropy of ARM and IRM were measured on various subsamples from 15556, 15016, 12017, and 10020 (see main text for details). Anisotropy ellipsoid parameters were computed following Stephenson (1986) (Table S8, S9).

7.2. Behavior of sample 15556,221c and relationship to ARM noise and anisotropy. In order to test whether the combined effects of magnetic anisotropy and spurious ARM are responsible for the flipping observed for 15556,221c, we employed the following procedure: We repeated AF applications multiple times along each orthogonal axis for all AF steps during demagnetization of NRM and measured the magnetic moment after each AF application. We counted how many times the magnetic moment flipped between antipodal directions for each AF level and determined the fraction of AF applications which led to flips. These counts were then binned

into groups by AF levels (bins range in size from 4-5 mT). The observed increase in flipping frequency with AF level up to 10 mT suggests that spurious ARM is responsible for the directional reversals during demagnetization because ARM noise strengthens relative to remaining NRM with peak AF field (Fig. S12).

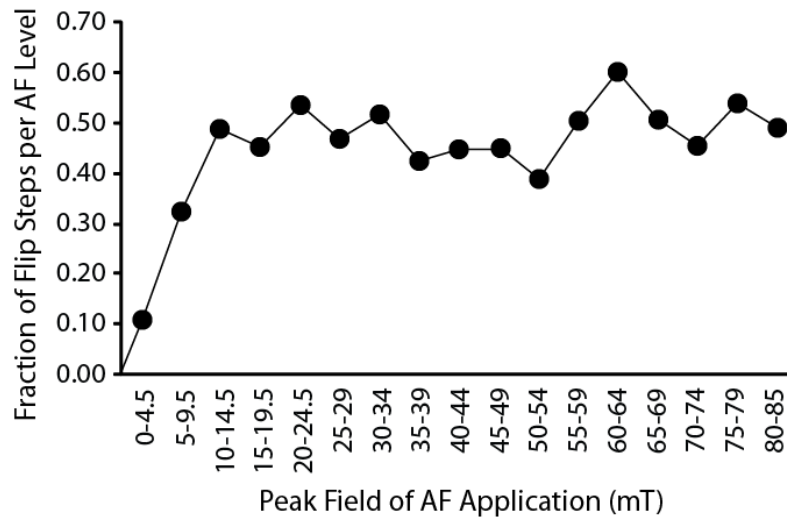


Figure S12. Frequency with which the magnetization of 15556,221c switched between antipodal directions during AF demagnetization. Data points signify the fraction of steps representing flips in moment for each range of AF levels shown on the abscissa.

Table S8. ARM anisotropy parameters.

Sample	Mass (mg)	<i>P</i>	<i>T</i>	<i>D</i> ₁ (°)	<i>I</i> ₁ (°)	<i>M</i> ₁ (Am ²)	<i>D</i> ₂ (°)	<i>I</i> ₂ (°)	<i>M</i> ₂ (Am ²)	<i>D</i> ₃ (°)	<i>I</i> ₃ (°)	<i>M</i> ₃ (Am ²)
15556												
221a	461.9	1.11	-0.42	344.4	59.2	4.29×10 ⁻⁸	245.1	5.6	3.98×10 ⁻⁸	151.8	30.2	3.87×10 ⁻⁸
221c	17.0	1.98	0.17	183.8	-59.3	4.66×10 ⁻⁹	162.2	29.6	3.60×10 ⁻⁹	257.4	9.4	2.35×10 ⁻⁹
221d	201.7	1.41	-0.71	258.8	-48.4	2.57×10 ⁻⁸	88.1	-41.3	1.91×10 ⁻⁸	174.0	4.7	1.82×10 ⁻⁸
221g	112.7	1.14	-0.04	64.2	-67.8	1.27×10 ⁻⁸	191.4	-13.8	1.18×10 ⁻⁸	285.8	-17.0	1.11×10 ⁻⁸
15016												
225B22	165.8	1.16	0.7	327.6	18.5	1.61×10 ⁻⁸	60.7	9.3	1.57×10 ⁻⁸	356.3	-69.2	1.38×10 ⁻⁸
12017												
12A1C	104.3	1.2	0.04	294.5	27.4	9.45×10 ⁻⁹	247.5	-52.8	8.65×10 ⁻⁹	191.6	23.1	7.85×10 ⁻⁹
13A2	49.5											
59	15.0	2.28	0.82	244.0	-12.4	1.09×10 ⁻⁸	149.2	-20.9	1.01×10 ⁻⁸	182.7	65.5	4.75×10 ⁻⁹
10020												
234b4	39.6	1.51	0.45	180.1	-43.0	1.36×10 ⁻⁸	1.2	-47.0	1.21×10 ⁻⁸	90.6	0.5	8.99×10 ⁻⁹

Note: The first column shows the subsample name. The second column shows subsample masses. The third column shows the average degree of anisotropy (*P*). The fourth column shows the average shape factor (*T*). The fifth through seventh columns display the declination, inclination, and length of the easy magnetic (*M*₁) axis. The eighth through tenth columns display the declination, inclination, and length of the medium (*M*₂) axis. The eleventh through thirteenth columns display the declination, inclination, and length of the hard (*M*₃) axis. Physically, axis lengths are the magnetic moments acquired along each axis from ARM and IRM acquisition during the anisotropy experiments in Am². Data for sample 10020 are sourced from Shea et al. (2012).

Table S9. IRM anisotropy parameters.

Sample	(mg)	<i>P</i>	<i>T</i>	<i>D</i> ₁ (°)	<i>I</i> ₁ (°)	<i>M</i> ₁ (Am ²)	<i>D</i> ₂ (°)	<i>I</i> ₂ (°)	<i>M</i> ₂ (Am ²)	<i>D</i> ₃ (°)	<i>I</i> ₃ (°)	<i>M</i> ₃ (Am ²)
15556												
221a	461.9	1.15	0.24	358.6	59.0	4.73×10 ⁻⁸	229.7	20.7	4.48×10 ⁻⁸	130.9	31.9	4.11×10 ⁻⁸
221c	17	2.6	0.30	185.5	-65.4	5.19×10 ⁻⁹	164.8	23.6	3.57×10 ⁻⁹	258.5	8.2	2.00×10 ⁻⁹
221d	201.7	1.56	-0.68	257.8	-37.4	3.21×10 ⁻⁸	84.5	-52.4	2.21×10 ⁻⁸	170.3	3.3	2.06×10 ⁻⁸
221g	112.7	1.18	-0.2	60.3	-24.9	1.13×10 ⁻⁸	36.9	63.2	1.02×10 ⁻⁸	145.9	9.4	9.56×10 ⁻⁹
15016												
225B22	165.8	1.19	0.38	5.5	8.7	1.98×10 ⁻⁸	97.7	14.0	1.87×10 ⁻⁸	64.5	-73.4	1.66×10 ⁻⁸
12017												
12A1C	104.3	1.38	-0.13	282.1	29.0	7.10×10 ⁻⁹	243.6	-54.8	5.91×10 ⁻⁹	181.6	18.3	5.13×10 ⁻⁹
59	15	2.23	0.86	253.3	-11.9	7.53×10 ⁻⁹	156.0	-30.4	7.12×10 ⁻⁹	182.0	56.0	3.38×10 ⁻⁹
10020												
234b4	39.6	1.93	0.5	182.4	-42.5	1.57×10 ⁻⁸	2.1	-47.6	1.34×10 ⁻⁸	92.2	-0.1	8.18×10 ⁻⁹

Note: The first column shows the subsample name. The second column shows subsample masses. The third column shows the average degree of anisotropy (*P*). The fourth column shows the average shape factor (*T*). The fifth through seventh columns display the declination, inclination, and length of the easy magnetic (*M*₁) axis. The eighth through tenth columns display the declination, inclination, and length of the medium (*M*₂) axis. The eleventh through thirteenth columns display the declination, inclination, and length of the hard (*M*₃) axis. Physically, axis lengths are the magnetic moments acquired along each axis from ARM and IRM acquisition during the anisotropy experiments in Am². Data for sample 10020 are sourced from Shea et al. (2012).

References

- Bailey, M., Dunlop, D., 1977. On the use of anhysteretic remanent magnetization in paleointensity determination. *Phys. Earth Planet. Inter.* 13, 360-362.
- Beatty, D., Albee, A., 1978. Comparative petrology and possible genetic relations among the Apollo 11 basalts. *Proc. Lunar Planet. Sci. Conf.* 9th 359-463.
- Buz, J., Weiss, B., Garrick-Bethell, I., 2011. Recent lunar magnetism. *Proc. Lunar Planet. Sci. Conf.* 42nd, 1675.
- Cisowski, S., Hale, C., Fuller, M., 1977. On the intensity of ancient lunar fields. *Proc. Lunar. Sci. Conf.* 8th 725-750.
- Cisowski, S., 1981. Interacting vs. non-interacting single-domain behavior in natural and synthetic samples. *Phys. Earth Planet. Inter.* 26, 56-62.
- Cisowski, S.M., Collinson, D.W., Runcorn, S.K., Stephenson, A., Fuller, M., 1983. A review of lunar paleointensity data and implications for origin of lunar magnetism. *Proc. Lunar Planet. Sci. Conf.* 13th A691-A704.
- Collinson, D.W., Runcorn, S.K., Stephenson, A., 1972. Magnetic properties of Apollo 15 rocks and fines, *The Apollo 15 Lunar Samples*, The Lunar Science Institute, Houston. pp. 425-429.
- Collinson, D.W., Morden, S.J., 1994. Magnetic-properties of howardite, eucrite and diogenite (HED) meteorites - Ancient magnetizing fields and meteorite evolution. *Earth Planet. Sci. Lett.* 126, 421-434.
- Cournede, C., Gattacceca, J., Rochette, P., 2012. Magnetic study of large Apollo samples: Possible evidence for an ancient centered dipolar field on the Moon. *Earth Planet Sci. Lett.* 331-332, 31-42.
- Crawford, D., Schultz, P., 1999. Electromagnetic properties of impact-generated plasma, vapor and debris. *Int. J. Impact Eng.* 23, 169-180.
- Dunlop, D., Bailey, M., Westcott-Lewis, M., 1975. Lunar paleointensity determination using anhysteretic remanence (ARM): A critique. *Geochim. Cosmochim. Ac.* 6, 3063-3069.
- Dunlop, D.J., Ozdemir, O., 1997. *Rock Magnetism: Fundamentals and Frontiers*. Cambridge University Press, New York. 573 pp.
- Egli, R., 2003. Analysis of the field dependence of remanent magnetization curves. *J. Geophys. Res.* 108, 2081.
- Fuller, M., Meshkov, E., Cisowski, S., Hale, C., 1979. On the natural remanent magnetization of certain mare basalts. *Proc. Lunar Planet. Sci.* 10th 2211-2233.
- Garrick-Bethell, I., Weiss, B., Shuster, D., Buz, J., 2009. Early lunar magnetism. *Science* 323, 356-359.
- Gattacceca, J., Rochette, P., Bourot-Denise, M., 2003. Magnetic properties of a freshly fallen LL ordinary chondrite: the Bensour meteorite. *Phys. Earth Planet. Inter.* 140, 343-358.
- Gattacceca, J., Rochette, P., 2004. Toward a robust normalized magnetic paleointensity method applied to meteorites. *Earth Planet. Sci. Lett.* 227, 377-393.
- Gattacceca, J., Boustie, M., Hood, L., Cuq-Lelandais, J.-P., Fuller, M., Bezaeva, N., de Resseguier, T., Berthe, L., 2010. Can the lunar crust be magnetized by shock: Experimental groundtruth. *Earth Planet. Sci. Lett.* 299, 42-53.
- Grove, T., Walker, D., 1977. Cooling histories of Apollo 15 quartz-normative basalts. *Proc. Lunar Planet. Sci. Conf.* 8th 1501-1520.

- Harrison, R., Feinberg, J., 2008. FORCinel: An improved algorithm for calculating first-order reversal curve distributions using locally weighted regression smoothing. *Geochem. Geophys. Geosyst.* 9, Q01056.
- Hoffman, K., Banerjee, S., 1975. Magnetic "zig-zag" behavior in lunar rocks. *Earth Planet. Sci. Lett.* 25, 331-337.
- Hood, L., Artemieva, N., 2008. Antipodal effects of lunar basin-forming impacts: Initial 3D simulations and comparisons with observations. *Icarus* 193, 485-502.
- Humphries, D., Biggar, G., O'Hara, M., 1972. Phase equilibria and origin of Apollo 15 basalts, etc, in: *The Apollo 15 Lunar Samples*, The Lunar Science Institute, Houston, pp. 103-107.
- Kirschvink, J., 1980. The least-squares line and plane and the analysis of palaeomagnetic data. *Geophys. J. Roy. Astr. S.* 62, 699-718.
- Kletetschka, G., Fuller, M., Kohout, T., Wasilewski, P., Herrero-Bervera, E., Ness, N., Acuna, M., 2006. TRM in low magnetic fields: a minimum field that can be recorded by large multidomain grains. *Phys. Earth Planet. Inter.* 154, 290-298.
- Lawrence, K., Johnson, C., Tauxe, L., Gee, J., 2008. Lunar paleointensity measurements: Implications for lunar magnetic evolution. *Phys. Earth Planet. Inter.* 168, 71-87.
- Morden, S.J., Collinson, D.W., 1992. The implications of the magnetism of ordinary chondrite meteorites. *Earth Planet. Sci. Lett.* 109, 185-204.
- Nagata, T., Fisher, R., Schwerer, F., Fuller, M., Dunn, J., 1972. Summary of rock magnetism of Apollo 15 lunar materials, *The Apollo 15 Lunar Samples*, The Lunar Science Institute, Houston. pp. 442-445.
- Nagata, T., Fisher, R., Schwerer, F., Fuller, M., Dunn, J., 1973. Magnetic properties and natural remanent magnetization of Apollo 15 and 16 lunar materials. *Proc. Lunar Sci. Conf.* 4th 3, 3019-3043.
- Pearce, G., Gose, W., Strangway, D., 1973. Magnetic studies on Apollo 15 and 16 lunar samples. *Proc. Lunar Sci. Conf.* 4th 3, 3045-3076.
- Pike, C., Roberts, A., Verosub, K., 1999. Characterizing interactions in fine magnetic particle systems using first order reversal curves. *J. Appl. Phys.* 85, 6660-6667.
- Rhodes, J., Blanchard, D., Dungan, M., Brannon, J., Rodgers, K., 1977. Chemistry of Apollo 12 mare basalts: Magma types and fractionation processes. *Proc. Lunar. Sci. Conf.* 8th, 1305-1338.
- Shea, E., Weiss, B., Cassatta, W., Shuster, D., Tikoo, S., Gattacceca, J., Grove, T., Fuller, M., 2012. A long-lived lunar core dynamo. *Science* 335, 453-456.
- Stephenson, A., Collinson, D., 1974. Lunar magnetic field paleointensities determined by an anhysteretic remanent magnetization method. *Earth Planet. Sci. Lett.* 23, 220-228.
- Stephenson, A., Runcorn, S., Collinson, D., 1977. Paleointensity estimates from lunar samples 10017 and 10020. *Proc. Lunar Planet. Sci. Conf.* 8th, 679-687.
- Stephenson, A., Sadikun, S., Potter, D., 1986. A theoretical and experimental comparison of the anisotropies of magnetic susceptibility and remanence in rocks and minerals. *Geophys. J. Roy. Astr. S.* 84, 185-200.
- Stephenson, A., 1993. Three-axis static alternating field demagnetization of rocks and the identification of natural remanent magnetization, gyroremanent magnetization, and anisotropy. *J. Geophys. Res.* 98, 373-381.
- Strangway, D., Pearce, G., Gose, W., Timme, R., 1971. Remanent magnetization of lunar samples. *Earth Planet. Sci. Lett.* 13, 43-52.

- Thellier, E., Thellier, O., 1959. Sur l'intensité du champ magnétique terrestre dans le passé historique et géologique. *Ann. Geophys.* 15, 285-376.
- Usselman, T., Lofgren, G., Donaldson, C., Williams, R., 1975. Experimentally reproduced textures and mineral characteristics of high-titanium mare basalts. *Proc Lunar Sci. Conf.* 6th, 997-1020.
- Weisberg, S., 1985. *Applied Linear Regression*. John Wiley and Sons, New York.
- Weiss, B., Berdahl, J., Elkins-Tanton, L., Stanley, S., Lima, E., Carporzen, L., 2008. Magnetism on the angrite parent body and the early differentiation of planetesimals. *Science* 322, 713-716.
- Yu, Y., Tauxe, L., Gee, J.S., 2007. A linear field dependence of thermoremanence in low magnetic fields. *Earth Planet. Sci. Lett.* 162, 244-248.
- Yu, Y., 2010. Paleointensity determination using anhysteretic remanence and saturation isothermal remanence. *Geochem. Geophys. Geosyst.* 11, Q02Z12.